ORIGINAL ARTICLE

lajss.org©
Latin American Journal of Solids and Structures
www.lajss.org

Numerical investigation into the effectiveness of steel i-beam strengthening techniques in steel-framed buildings

Alhammadi, S.A.[a]*

[a] Vice Rectorate for Facilities and Operation, Princess Nourah bint Abdulrahman University, P.O. Box 84428, Riyadh 11671, Saudi Arabia. E-mail: saalhammadi@pnu.edu.sa

*Corresponding author

https://doi.org/10.1590/1679-78256696

Abstract

While structural strengthening is not the consequence of a structure's condition of failure, it does take place as a result of a need to increase the structural stiffness and load capacity when a change in the structure's usage occurs. As a result, various techniques must be presented to enhance the structural elements by considering economic and time requirement factors and load-bearing capacity. In this study, the issue is demonstrated using a steel I-beam that was strengthened using six different techniques to postpone the beam's lateral torsional buckling to achieve its full plastic flexural capacity. Finite element (FE) analyses were carried out with the use of Abaqus software to predict the response of both unstrengthened and strengthened steel I-beams in a four-point bending test for a total of 56 specimens with different parameters studied. In order to understand which strengthening techniques are most appropriate for a new or existing steel building, an analysis of the costs was conducted for each strengthening technique to reach a conclusion regarding which strengthening techniques would be ideal for use.

Keywords

strengthening; finite element models; steel beam; lateral torsional.

Graphical Abstract

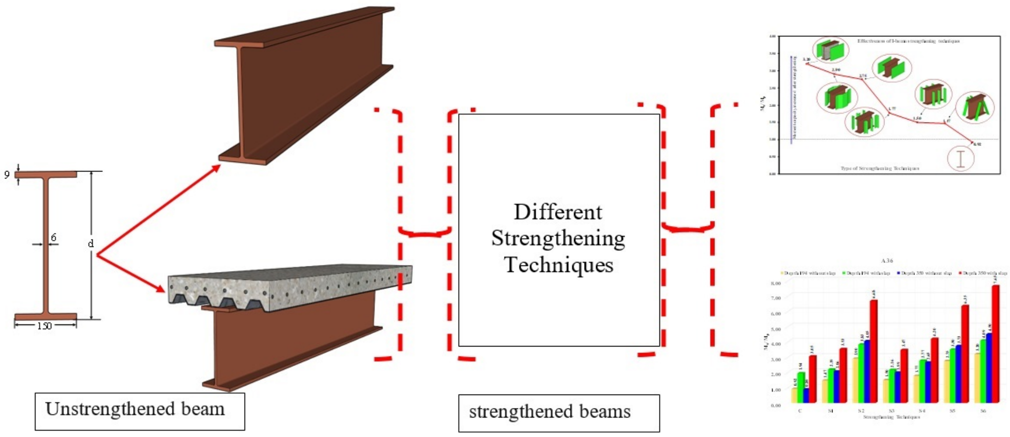

Received August 11, 2021. In revised form September 10, 2021. Accepted September 13, 2021. Available online September 16, 2021
https://doi.org/10.1590/1679-78256696

1 INTRODUCTION

In recent decades, the authors' attention has been drawn to the strengthening of reinforced concrete (RC) and steel buildings. Strengthening techniques are used to describe retrofit work that involves the addition of a material to a base cross-section in order to transfer additional load.

In accordance with the width-to-thickness ratios of the web and the flanges, steel I-sections subjected to flexure are defined as compact and non-compact sections (Sayed-Ahmed, 2006). Compact sections are capable of developing the cross-section full plastic moment, whereas non-compact sections are only guaranteed to develop the cross-section yield moment. The use of structural steel has its limits, however, and one of those constraints is the possibility of laterally torsional buckling (Yossef,2015), especially when the compression flange of the steel section is thin and/or the beam is not properly restrained. The lateral torsional buckling, in unrestrained steel I-beams is a significant aspect of structural behavior in steel structures, and many experimental and numerical studies have been carried out by many researchers over the past decades to better understand this phenomenon (Timoshenko and Gere, 2009; Dibley, 1969; and Kabir et al., 2020).

Yossef (2015) conducted an experimental investigation on the behavior of strengthening steel beams. Six specimens were subjected to full scale testing after being strengthened with steel cover plates. The findings indicated that the length of the cover plate had an effect on the final load carrying capacity of the specimens tested. Additionally, the area of the welded plate had an effect on the final load carrying capacity. An experimental investigation into W-shaped beams strengthened while under load was performed by Liu and Gannon (2009). W-shaped beams were evaluated with a four-point load test. The authors found that the preload level, during loading, had an effect on beam load deflection during beam failure. There have been many studies on the use of FRP composites for strengthening steel I-beams (Al-Saidy et al., 2004; Nozaka et al., 2005; and Al-Ridha et al., 2019). However, this may have many drawbacks, such as being affected by high temperatures or direct fire. Six beams were subjected to a range of experimental and analytical research studies by Sen et al. (2001) to discover if CFRP strips might be used to repair steel–concrete composite beam members. It was observed that the bonding technique had a greater effect on the repair than did the CFRP thickness. According to Kabir et al. (2021) and Feng et al. (2018), an alternate encasement design, including the use of different engineered cementitious composites and also light-weight concrete, was shown to be effective in the prevention of both local and lateral torsional buckles.

Attempts have been made to describe the key advances in experimental and numerical studies that led to the generally accepted techniques in contemporary design guidelines and codes of practice. However, the lateral torsional buckling problem still exists, especially when the steel I-beams are subjected to additional loads that were not designed in advance, and this prompts us to develop strengthening techniques for existing or new steel buildings to reduce this problem. Thus, in this study, we used 56 steel I-beams divided into seven groups, where the first group was unstrengthened beams (control specimens) and the rest of the six groups were strengthened using different techniques. Each group included study parameters in terms of studying two types of steel materials: A36 and A572, as well as studying two different depths of the steel I-beam, in addition to studying the beams with and without composite floor slabs. To study the interaction of these strengthening techniques and their effects on the steel I-beam, nonlinear finite element (FE) models using Abaqus software (2020) were developed to predict the response of both unstrengthened and strengthened steel I-beams in a four-point bending test. The models were validated by calibrating the FE models with two steel I-beams that had been tested experimentally by Kabir et al. (2021) and Feng et al. (2018). We were able to assess the appropriateness of each strengthening technique in terms of cost versus load-bearing capability using the strengthening schemes.

2 NUMERICAL STUDY

This section presents the numerical program developed with the Abaqus software (2020) to investigate the effectiveness of steel I-beam strengthening techniques. The program was based on the calibration and verification of experimental tests obtained from the literature and presented in this paper. FE analysis is a popular numerical method for solving partial differential equations in order to find approximate solutions to boundary value problems.

The adopted model is described in eight different groups: (i) mesh discretization, (ii) boundary condition, (iii) loading, (iv) material model calibration, (v) initial imperfections, (vi) analysis procedure, (vii) FE model validation, and (viii) models for the parametric analysis.

2.1 Mesh discretization

The FE geometry for a steel I-beam is shown in Figure 1. For various parts, solid elements with eight nodes and reduced integration (C3D8R) were used (beams, plates, slab, and steel plate for strengthening). For the corrugated steel sheet, S4R (shell element) with four nodes and reduced integration was used. The S4R element had six degrees of freedom thanks to three rotations and three translations for each node. T3D2 two-node linear three-dimensional truss elements were used to make the reinforcing bars (Rossi et al., 2020).

Mesh sensitivity analysis was used to determine appropriate element sizes for various components. The web of a steel beam was partitioned into at least 9 elements along its height, with a maximum element size of 20 mm. All steel beam flanges were partitioned into at least 8 elements along their width, with a maximum element size of 20 mm. The stud element size was chosen to be 4 mm. Reinforcement bars were meshed with a 100 mm element size. The size of the concrete elements ranged from 15 to 25 mm. Because it is in direct contact with the concrete, this mesh was also used for the corrugated steel sheeting.

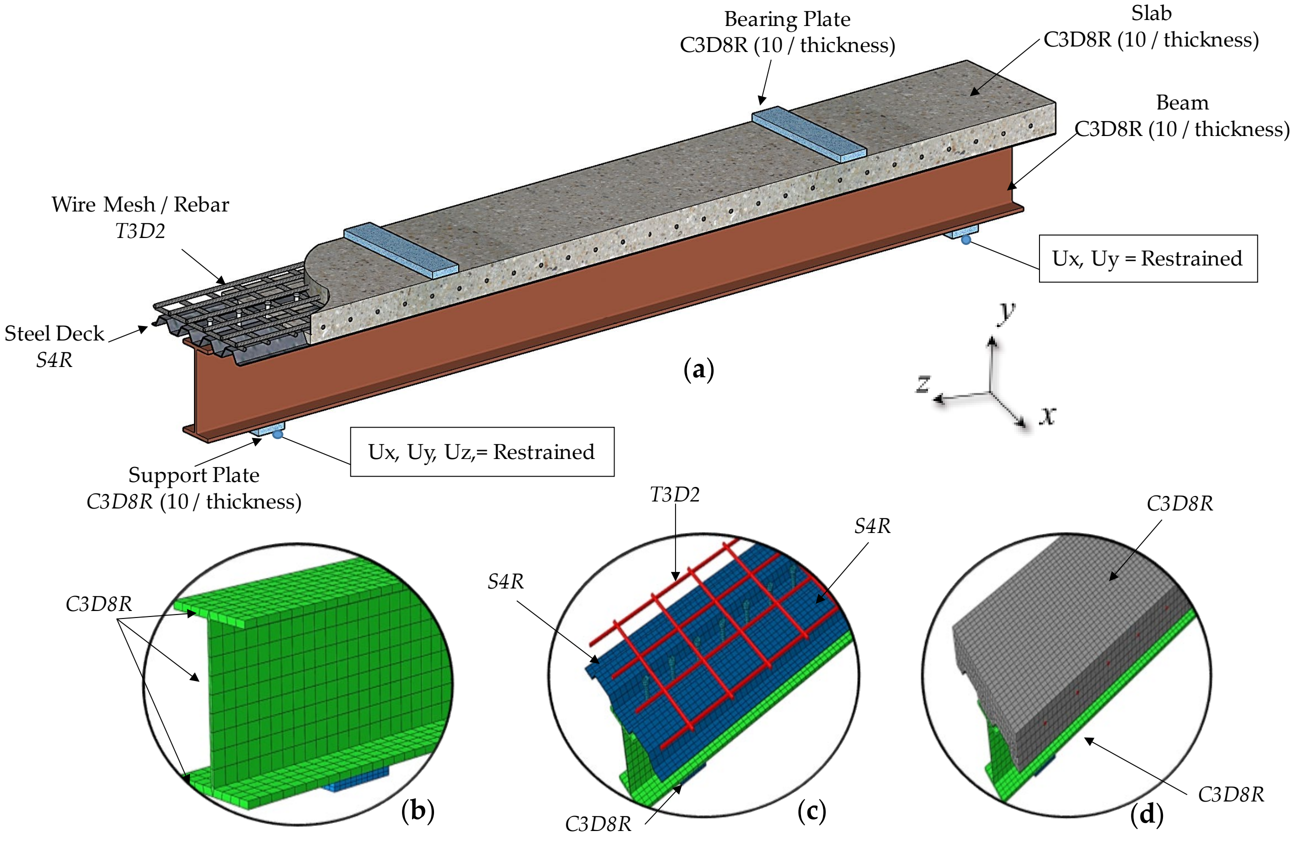

Figure 1 (a) FE model specifics for a typical subassembly configuration with composite floor slab; (b) steel I-beam detail; (c) reinforcement bars, shear stud, and steel deck detail; and (d) slab detail.

2.2 Boundary conditions

With respect to the boundary conditions, the nodes on each support or loading line were restricted to a reference point (the support point or loading point in this research) through kinematic coupling in simulating the boundary conditions of the test (Figure 2). One of the supports was pinned, and the other support was set as a roller. In order to model the load displacement control, a control displacement versus time function was input to the two-point load on the steel I-beam. It was decided that the interaction between components should be of a general contact type between element specimens. At first contact, the coefficient of friction was considered to be 0.3 between steel components (Dinu et al., 2017). Simulated welds were created by creating a "tie" contact interface.

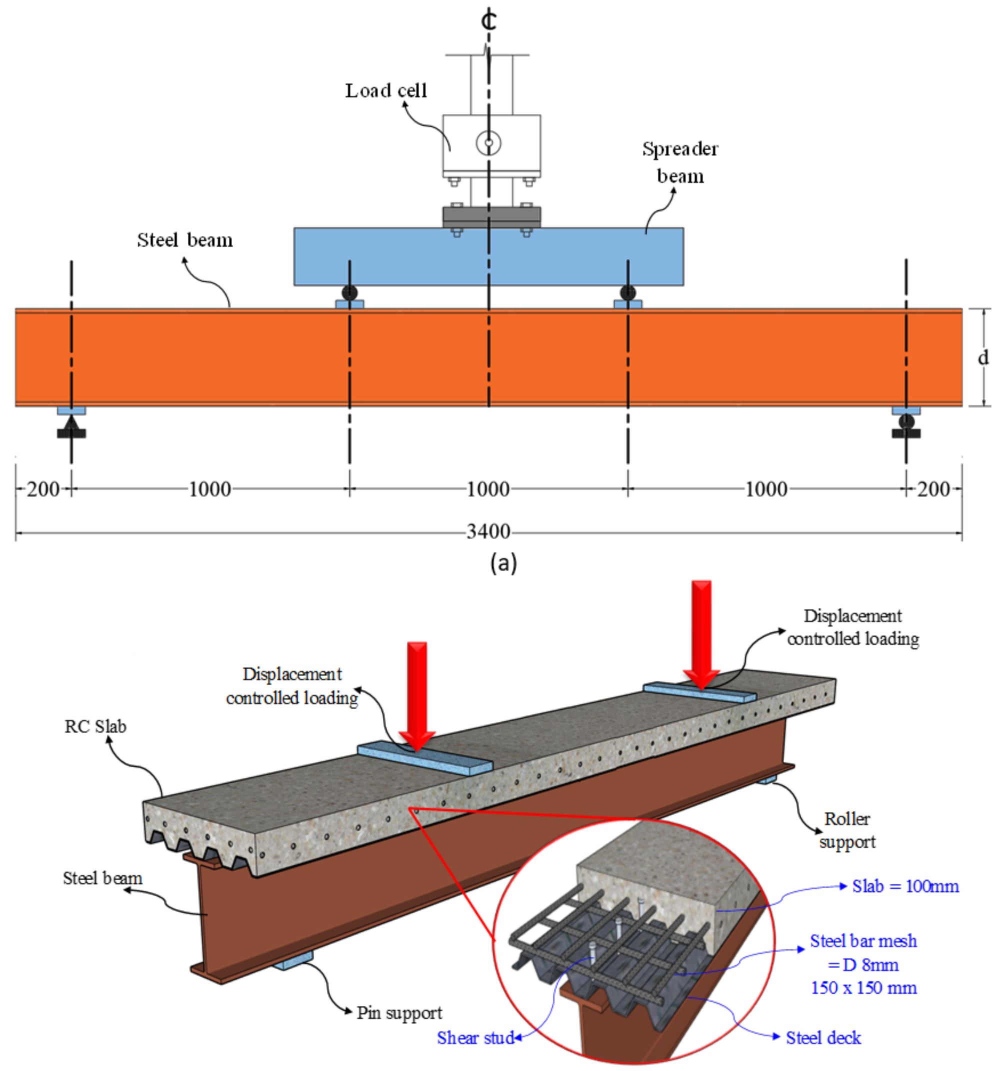

(a)

(b)

Figure 2 Dimensions and detailing of FE analysed steel I-beam (Note: All dimensions are in mm): (a) Elevation of the typical steel I-beam; (b) Boundary and loading conditions of a typical steel I-beam with slab.

2.3 Loading

Abaqus uses explicit time integration algorithms to solve problems. The load application process in Abaqus is time history dependent. The displacement controlled node set was given a constant velocity because the testing procedure involved displacement controlled static loading (Figure 2). To reduce the solution time, the displacement rate of change was set to 10 mm/s, which could represent quasi static dynamic loading. In this case, the inertia force developed is considered marginal and has no effect on the FE modeling results. Furthermore, in the material models, the strain rate effects associated with the dynamic explicit analysis were disabled.

2.4 Material model calibration

A36 and A572 G50 steel materials were modeled using tensile tests carried out on coupons obtained from identical steel plates and beams, which were then utilized numerically to create all steel I-beams and strengthening materials (ANSI/AISC 360-16, 2016). The engineering stress–strain curves for coupons in the same batch were nearly identical, so only one curve was used to process each material. Stress and strain are generally presented in terms of engineering stress–strain (σ_{eng} - ε_{eng}). In order to use these numbers for the numerical modeling, the engineering stress–strain (σ_E - ε_E) was calculated and transformed into true stress and logarithmic plastic strain (σ_{true} - $\varepsilon_{(pl/ln)}$) up to the maximum load using the following equations [1,2]:

$$\sigma_{true} = \sigma_{eng} (1+ \varepsilon_{eng}) \tag{1}$$

$$\text{å}_{\underline{pl}\atop ln}=\ln(1+ \varepsilon_{\text{eng}}) - \frac{\text{ó}_{\text{true}}}{E} \tag{2}$$

For tensile tests on coupons, FE models were built in Abaqus (2020), and the actual measurements of the specimens were used (Figure 3). Figure 3 (a) shows a model of the coupon outside the grasp. Kinematic restraints were assigned to the ends of the coupon, and reference points were linked to them. While one reference point remained fixed in all degrees of freedom (the static grip), another reference point experienced longitudinal displacement as a result of an explicit step in the simulation model (the moving grip). When designing this specimen, the mesh size was chosen to be the same as the mesh used in the materials models in the potentially plastic regions.

Apart from the true stress–plastic strain curve, material density, Poisson's ratio, and the Young's modulus, ductile damage as used in the material model, which is defined by fracture strain and stress triaxiality (Abaqus 6.20, 2020; Yan et al., 2018; and Dinu et al., 2017) (see Table 1). To match the decreasing form of the engineering stress–strain curve, the polynomial parameters for the true stress–true strain relationship were changed to take into account the maximum force. This is seen in Figure 4, where the true stress and true strain curves for materials (A36 and A572) are shown. Figures 3 (b) and 5 illustrate a comparison of experimental and FE failure mechanisms for samples of A36 and A572 steel coupons subjected to standard testing. There was a high degree of agreement between the results of the experimental and FE failure mechanism s, but the elastic modulus has some disagreement. This could be due to a number of aspects, the most important of which is that the experimental side is not ideal in the readings, where the readings and loading are subject to factors that cannot be completely controlled, unlike the numerical. The geometrical properties of the sample may be uncontrolled on the experimental side as long as they are accurately represented on the numerical side, and there must be a difference between the practical and the numerical in all experiments. This demonstrates the accuracy with which both element size and input material characteristics capture steel fracture through element erosion. Thus, in the FE parametric analysis specimens, the calibrated element size was utilized.

Modeling concrete was accomplished via the use of the concrete damage plasticity model (CDPM) in this research. CDPM is widely used to represent the complex behavior of quasi-brittle materials such as concrete, and it is very versatile. Using this model, one can simulate the behavior of concrete under both monotonic and cyclic loads (Lee and Fenves, 1998). The elastic and plastic characteristics of concrete are involved in the stress–strain response of the material. The total strain of concrete is the sum of all of the elastic and plastic stresses in the concrete. The plasticity and damage response of concrete are represented by the nonlinear part of the stress–strain response of concrete. As a result, it is critical to identify the kind of damage caused by the plastic strain of the concrete. Damage variables in concrete are represented by d_c and d_t, which stand for compression and tension damage, respectively. The level of the damage is assigned a number between 0 and 1. In this case, 0 indicates no damage, while 1 represents complete damage (Lakavath et al., 2021; Lee and Fenves, 1998; Yu et al., 2010; and Chi et al., 2014). The yield criteria describe the critical stress level beyond which plastic deformation begins to occur and ultimately results in failure. The strength under compression and tension [Lee and Fenves, 1998; and Lubliner et al., 1989) has been the focus of many studies. Using a similar technique, CDPM in Abaqus (2020) employs a complex polynomial solver. As concrete in various circumstances was tested, only a few researchers could create failure envelopes. Some information on CDPM is covered in this paper, and more information about it may be obtained elsewhere (Abaqus, 2020). Dilation angle, eccentricity, stress ratio, shape factor, and viscosity parameter are all values of concrete that are given in Table 2.

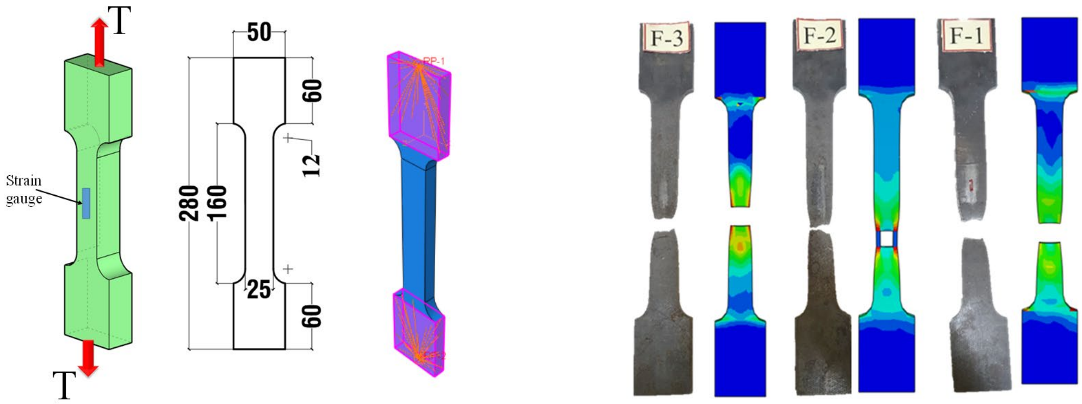

(a)

(b)

Figure 3 Details of material model calibration: (a) Details coupon test; (b) Experimental and FE mode of failure.

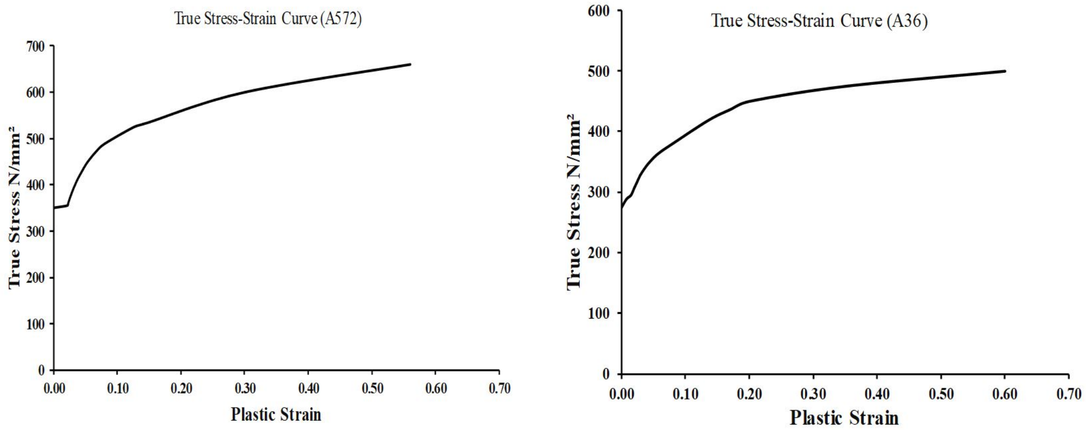

(a) (b)

Figure 4 True stress vs plastic strain graph for coupon plate specimens (a) A570 materials; (b) A36 materials.

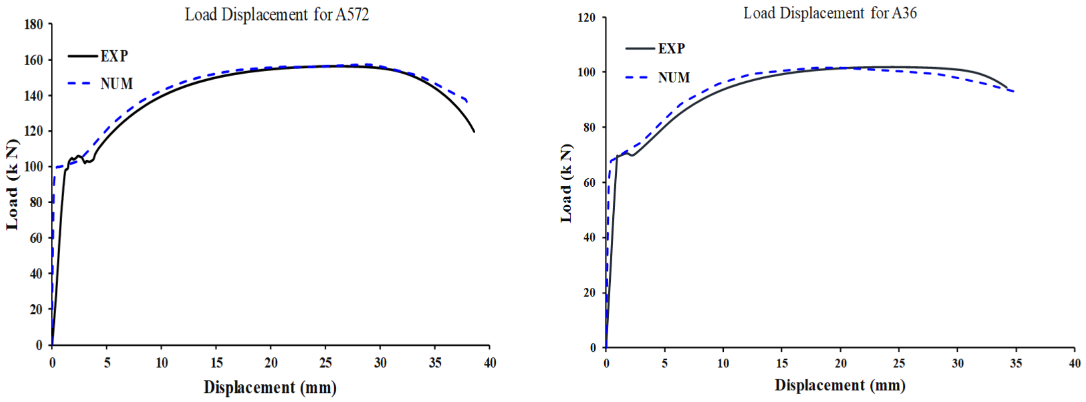

(a) (b)

Figure 5 Comparison of load vs displacement response for coupon plate specimens (a) A570 materials; (b) A36 materials.

Table 1 Input parameters for material models used in the FE modeling.

Component	Material properties of steel					
	Elastic and plastic properties				Coefficients used for ductile damage model*	
	Yield strength f_y (MPa)	Tensile strength f_u (MPa)	Elongation at fracture ä (%)	Elastic modulus E (GPa)	Fracture strain	Stress Triaxiality
A36 for beam and steel plates	273	446	23	194	0.60	0.82
A572 for beam and steel plates	357	462	23	196	0.56	0.80
Reinforcement bars	423	522	23	202	0.54	0.78
Headed stud	320	400	0.14	200	0.57	0.80
Steel deck	320	380	0.38	201	0.57	0.80

*Ductile damage criteria depend on the mesh size and shape as well (Abaqus 6.20, 2020; Yan et al., 2018; and Dinu et al., 2017).

Table 2 Mechanical properties for concrete used in the FE modeling.

Compressive strength (MPa)	Elastic		Plastic				
	Elastic Modulus (MPa)	Poisson’s ratio	Dilation angle (ö)	Eccentricity (ϵ)	Fbo/Fco	K_c	Viscosity Parameter (μ)
30	30588.5	0.15	36	0.1	1.16	0.667	0.0005

2.5 Initial imperfections

For imperfections, two types of specimens from the literature were chosen for validation: one without a slab (TQ-HW-d0-B4 tested by Feng et al. 2018) and one with a slab (E30-p tested by Kabir et al. 2021), in order to account for residual stresses and initial geometric imperfection deficiency and apply it to this type of steel beam in this study.

In terms of residual stresses, as a consequence of varying cooling rates in different parts of a steel beam, welding or hot rolling the material may result in a significant amount of residual stress, resulting in nonlinear material characteristics sooner (Shayan et al., 2012). As a result, when modeling pure steel beams (without slab) using the FE technique, it is common practice to include the existence of residual stresses. The ECCS (1984) model is used in this study to characterize the longitudinal residual stress distribution (σ_R) in steel beams. Initial stresses in the steel beam's web and flange components were generated by utilizing preset ABAQUS features to add longitudinal residual stresses to the model. The model was verified against experimental results from Kabir et al. (2021) and Feng et al. (2018), and was then used to perform a parametric analysis of a variety of strengthening techniques. Simple steel beams with slabs or strengthening methods are mostly under tension, and it seems as if composite slabs and strengthening techniques significantly reduce the effect of residual stresses. This is consistent with results of Ban et al. (2016) and Katwal et al. (2018). According to sensitivity analysis, after adding residual stresses, the predicted ultimate load is decreased by less than 1%. Although residual stresses have a minor effect on prediction accuracy, they were included in the FE modeling since the steel beam's initial stress conditions are reasonably straightforward to account for.

With respect to the initial geometric imperfections, it is widely accepted that initial geometric imperfections can have a significant influence on pure steel beams, because the presence of the imperfections can promote lateral torsional buckling. Because the restraint from the concrete slab normally prevents lateral-torsional buckling of the steel beam in a composite beam under sagging moments, the geometric imperfection that was considered was local buckling within the portion of the steel beam in compression. A separate model was analyzed prior to the loaded beam analysis to determine the Eigen modes of the beam to be used as an initial imperfection for the mechanical loaded model. Using the command *IMPERFECTION to update the coordinates of selected nodes, the application of initial geometric imperfections in ABAQUS was archived.

For composite beams, local buckling was applied at the mid-span in accordance with an eigenvalue local buckling mode with an amplitude of 1% of the width of the steel beam or 3 mm, whichever is larger, as specified on the tolerance of out-of-square prescribed in EN 10034 (1993). The FE model with applied local geometric imperfections is shown in Figure 6 (a) at an 8:1 scale. As shown in Figure 6 (b), the existence of initial imperfections has no discernible effect on the composite beam's initially response during model validation. After achieving a mid-span deflection of about 35 mm (equal to L/97, where L is the span length), a small decrease in load bearing capacity is noticed as a result of the initial imperfections' effect. However, at a mid-span deflection of 50 mm (equal to L/68), this specimen's maximum strength loss is just 2.0%. Katwal et al. (2018), as well as the majority of research in the literature, found that initial imperfections had a minimal effect on simply-supported beams with slabs. Similarly, since the experiments were conducted on strengthened simply-supported beams, the effect of initial imperfections on these beams is minimal. This result is also compatible with those of Kabir et al., (2021 and 2020), Ban et al., (2016), Katwal et al., (2018), and Feng et al., 2018. Because it is more essential to address concrete deterioration than initial imperfections, initial imperfections are ignored in FE modeling of strengthened and composite beams to simplify beam simulation.

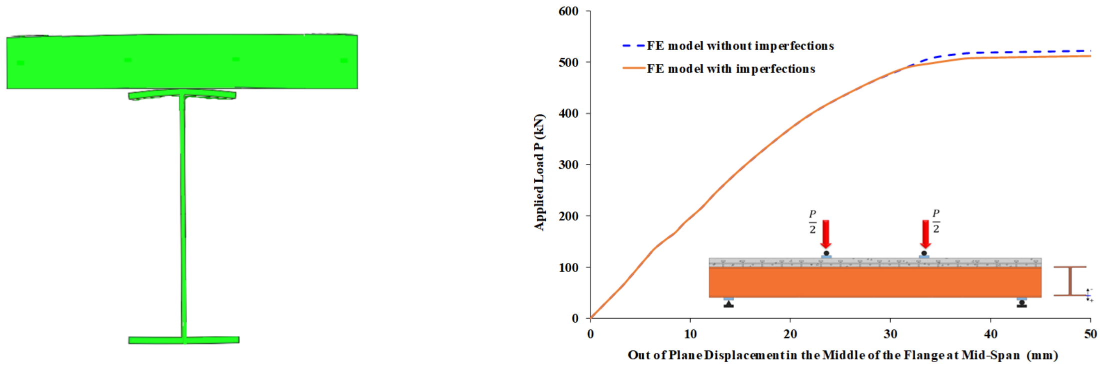

(a) Cross-section of initial geometric imperfections being applied (scale 8:1)

(b) Effect of imperfections on load displacement curves.

Figure 6 Effect of initial imperfections on E30-p specimen tested by Kabir et al. 2021.

The analysis of modal shapes for a steel beam without a slab (TQ-HW-d0-B4 specimen tested by Feng et al. 2018) revealed translational, torsional, or local displacement, as shown in Figure 7. The numerical model for the mechanically loaded beam was modified using Keyword editing with the normalized deformed shape of the beam, introducing successively the deformed shapes obtained as the first three Eigenmodes. In accordance with CEN, prEN (1993), the scale factor used for the global initial deformation was l/1000. The inclusion of the first mode as an initial imperfection resulted in a response curve that was comparable to the experimental curve.

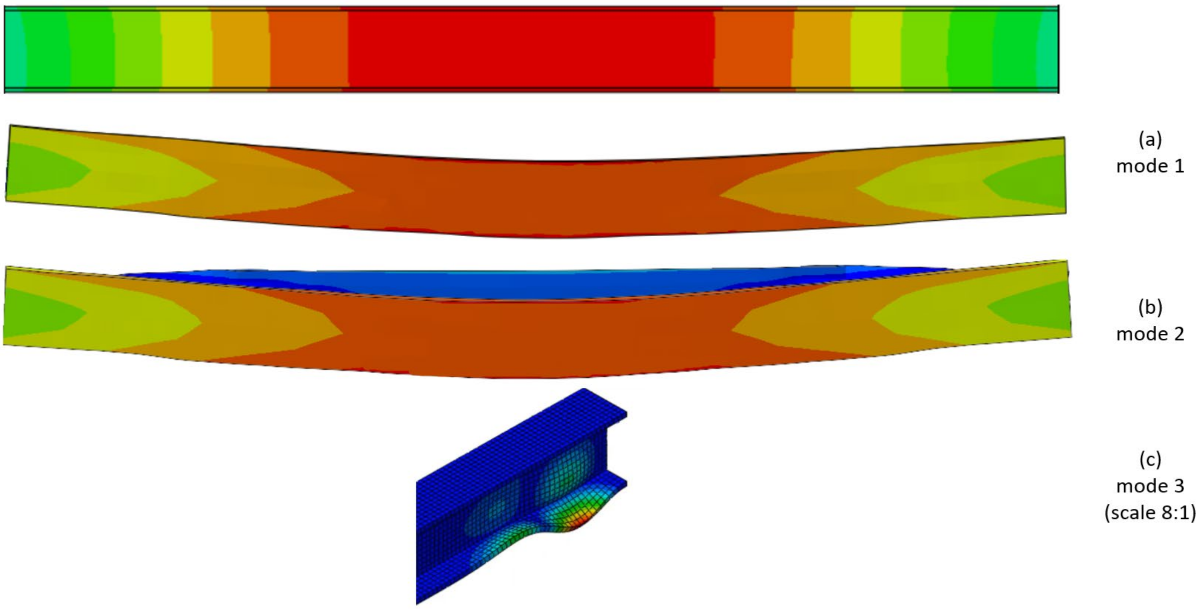

Figure 7 Eigenmodes: a) First eigen buckling mode, b) Secand eigen buckling mode, c) Thired eigen buckling mode-local.

2.6 Analysis procedure

Convergence is always difficult to achieve when using the “General Static” approach in ABAQUS due to the complex interaction between different components in a steel I-beam. Instead, the “Dynamic Explicit” approach was used in this study to accelerate convergence. Because the simulation is only for static tests, it is necessary to ensure that the dynamic effects in the FE analysis are negligible by comparing the kinetic energy (KE) of the entire model with the internal energy (IE) of the entire model. In all cases, it was discovered that KE was less than 5% of IE. As a result, according to the ABAQUS User's Manual (2020), any dynamic effects resulting from the analysis can be ignored (Katwal et al., 2018).

2.7 FE Model validation

Kabir et al. (2021) and Feng et al. (2018) conducted experiments on two different specimens, and the findings of these experiments were utilized to validate the FE models. In order to test the compatibility of this study with the study parameters, these two studies were chosen in which one included the beams with the slab (Kabir et al., 2021 (Figure 8(a))) and one did not include the slab (Feng et al., 2018 (Figure 8 (b))). The results of the FE model validation are discussed in terms of load-displacement response and mode of failure. Figure 9 shows a comparison of the observed and numerically predicted key load-displacement findings for the two test steel I-beams. The numerically predicted failure modes of the two test steel I-beams are shown in Figure 10, and it can be seen that they are in good agreement with the results of the tests. The comparisons between measured and predicted load against mid-span displacement for the two test steel I-beams are shown in Figure 9, and a fair match was observed between the experimental and numerically predicted curves, particularly for the ultimate load. As shown in Figure 9, the stiffness of the test steel I-beams was numerically well evaluated when compared to the tests. The FE models were similarly accurate in predicting the descending part of the load-displacement response, shown in Figure 10, demonstrating the accuracy of the constitutive modeling. As a result, the numerically generated models were calibrated for both the free steel I-beam and steel I-beam with slab, and they were then able to be used to investigate the behavior of various strengthening methods on steel I-beams under four-point bending tests, as will be described in the next section.

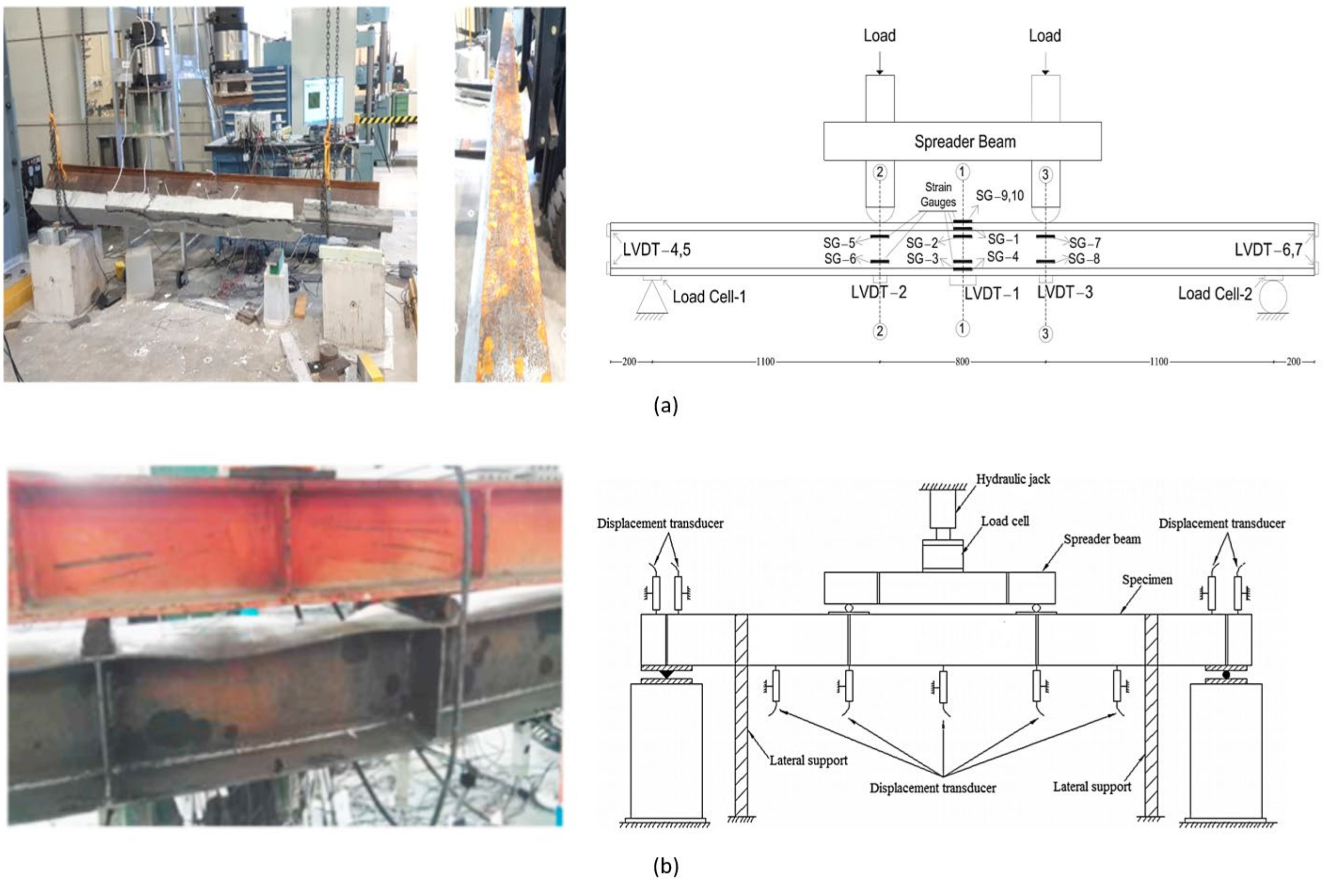

(a)

(b)

Figure 8 Details of steel beams specimens for validating the FE analysis (Dimensions are measured in mm): (a) Assembly E30-p tested by Kabir et al. 2021; (b) Assembly TQ-HW-d0-B4 tested by Feng et al. 2018.

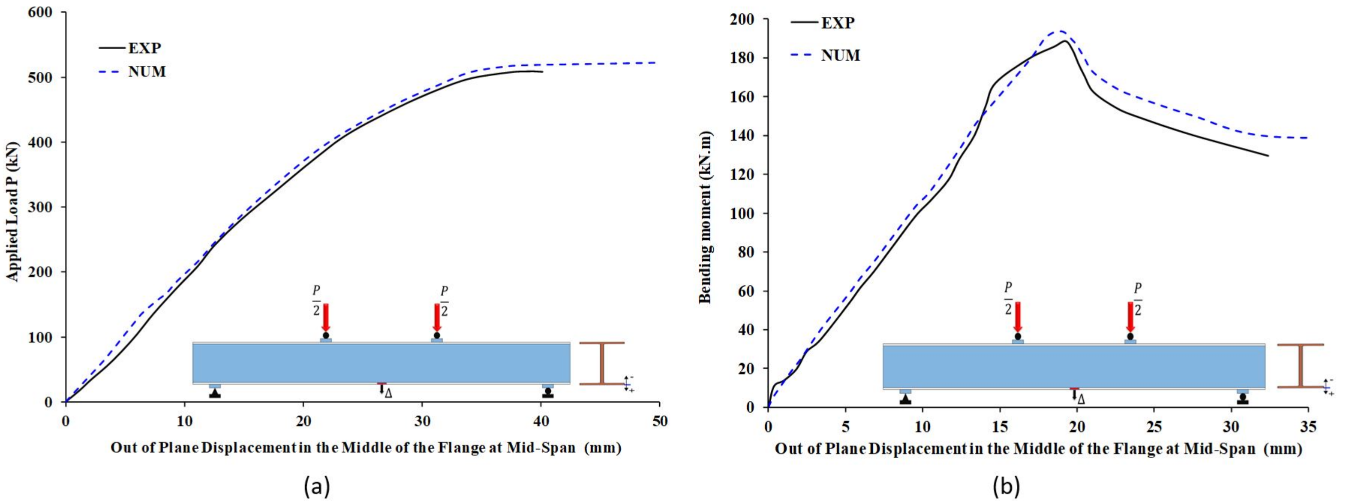

(a)

(b)

Figure 9 Comparison of load vs displacement envelopes for: (a) Assembly E30-p tested by Kabir et al. (2021); (b) Assembly TQ-HW-d0-B4 tested by Feng et al. (2018).

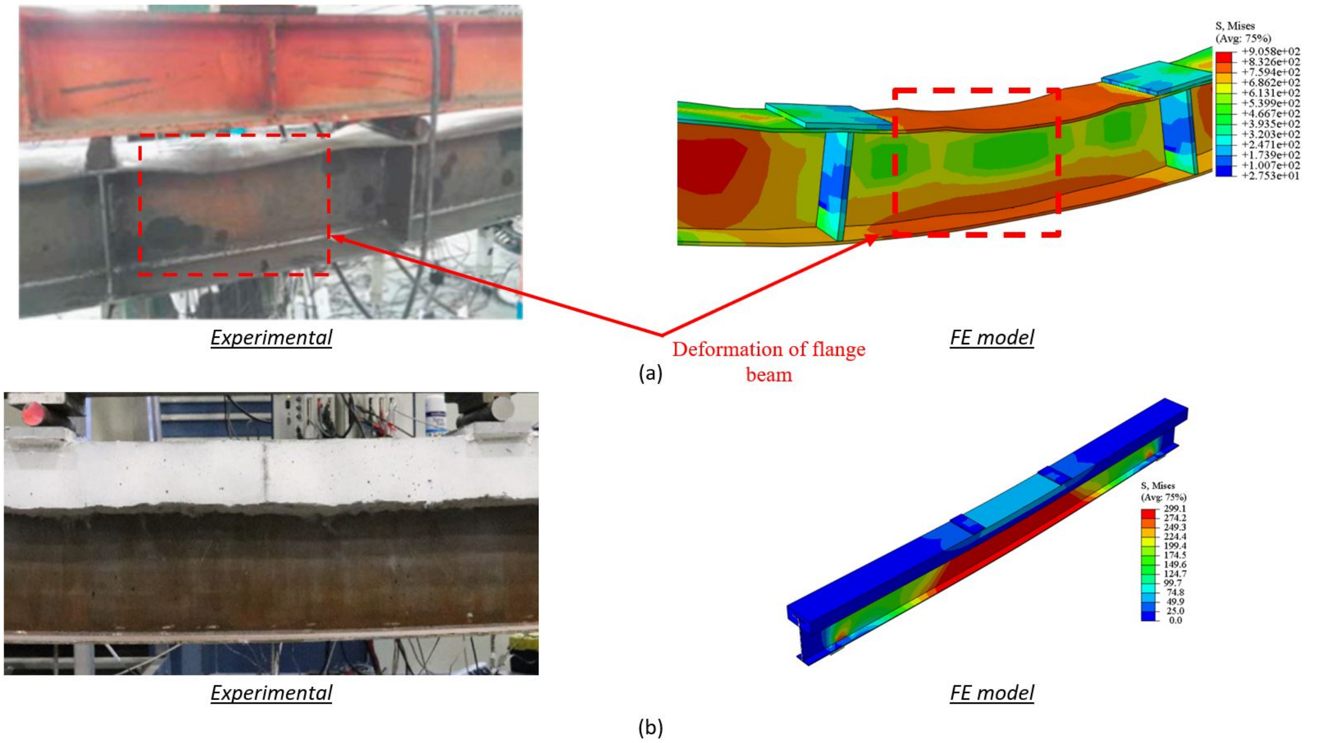

Figure 10 Numerically predicted failure mode for: (a) Assembly E30-p tested by Kabir et al. (2021); (b) Assembly TQ-HW-d0-B4 tested by Feng et al. (2018).

2.8 Models for the parametric analysis

The efficacy of the strengthening techniques is the primary focus of this research, which is to ensure that they are successful in all instances of steel I-beams. Four main parameters were thus proposed: the steel grade, effects caused by the composite floor slab, the depth of a beam, and six different types of strengthening techniques. The first parameter is the steel grade, which was used to determine how to affect the steel I-beam in its strengthened or unstrengthened condition, as well as with all of the different techniques of strengthening. The steel grades that were used are ASTM (2014), and these are the two types of materials that are most commonly used in local steel facilities. In this study, these two types of materials were used with all steel I-beams, as well as with materials that are used in the strengthening techniques. The second parameter is the effect of the composite floor slab on the steel I-beams and whether the steel I-beam was unstrengthened or strengthened with the six techniques; additionally, we considered the effect of the composite floor slab when other parameters such as material strength (steel grade) and beam depth were changed (Figure 1 and 2). The third parameter is the change of the steel I-beam in two different depths so that it has a compact and noncompact section, and this is of paramount importance in determining whether the beam will reach its full plastic moment in the case of beams unstrengthened or strengthened with the six techniques, as well as when using a beam with or without a composite floor slab and when using different steel grades (see Table 3).

Table 3 Details of parametric study.

Parametric study	Description
Steel grade	ASTM (2014)
	ASTM (2014)
Depth of beam	194 mm
	350 mm
Composite floor slab	Steel I-beam with composite floor slab
	Steel I-beam without composite floor slab
Strengthening techniques	Six different types of strengthening techniques.

The FE analysis was conducted in Abaqus (2020) to investigate the fourth parametric which is the effectiveness of steel I-beam strengthening techniques in steel-framed buildings. The geometric dimensions for steel I-beams are shown in Figure 1 and in Table 4. Details of the parametric analysis used in the numerical program are presented in Table 5. The numerical program of this research comprised testing up to the failure of a total of 56 simply supported steel I-beams under four-point loading. The FE parametric analysis was divided into seven groups with different parameters, such as: the steel grade, effects caused by the composite floor slab, and the depth of a beam (see Table 5). Out of the seven groups, the first group (Group 0) was unstrengthened control I-steel beams (see Figure 11). This group (Group 0) sought to identify the weaknesses of the beams in existing buildings before strengthening them. Through this group, it was possible to compare the performance of the unstrengthened group with the strengthened groups (Group S1 to Group S6). The second group (Group S1) was the same as the control specimens (Group 0); however, the steel I-beams were strengthened using a diagonal stiffener plate welded to the web of the beam (see Figure 12). The third group (Group S2) was the same as the control one, but it was strengthened using a corrugated plate welded to the web of the beam (see Figure 13). As for the fourth group (Group S3), it was similar to the first (Group 0), but it was strengthened using vertical stiffener plates welded to the web of the beam (see Figure 14). The fifth group (Group S4) was also similar to the first group, but it was strengthened using an angle stiffener welded to the web of the beam (see Figure 15). The sixth group (Group S5) was the same as the control one, but it was strengthened using welded side plates along the inner side of the flanges of the beam (see Figure 16). The last group (Group S6) was similar to the Group S5, but it was strengthened using partially encased concrete along with the web of a beam (see Figure 17).

Two meshes with a diameter of 8 mm and G60 material were used to reinforce a 500x100 mm composite floor slab made of C30 concrete. The steel I-beam had the dimensions of 194×150×9×6 mm and 350×150×9×6 mm. Shear studs, which were 10x75mm in size, were used to achieve the connection between slab and beam. The beam had a length of 3.4 meters (see Figure 2 and Table 4). The locally available ASTM A36 and A572 G50 steel were used in the design. The dimensions and thicknesses of the strengthening techniques were designed based on the geometrical shape of the steel I-beam, so that it fits all of the different configurations of the steel I-beams, as shown in Figures 11 to 17. By means of analyses based on numerous dimensions and variable geometries, the best strengthening models from these analyses were selected, and their results are presented in this study. The proposed strengthening techniques are simple and easy to implement. The implementation of all the proposed strengthening schemes caused substantial enhancement in the moment of inertia and shear area in the beam.

Table 4 Details of beams utilized for FE analysis validation. *

Reference	Specimen ID	Beam I-section D × B × t_f × t_w (mm)	Concrete section (mm)	Overall length (mm)	Yield strength f_y (MPa)	Ultimate strength f_u (MPa)
Kabir et al. (2021)	E30-p	310 × 110 × 6 × 6	210 × 92.5	3400	759	856
Feng et al. (2018)	TQ-HW-d0-B4	225× 125 × 6× 6	-	2300	677.9	725.8
FE Current study	Specimens with depth 194 mm	194×150× 9× 6	Specimens with slab 500 × 100	3400	See Table 1	See Table 1
	Specimens with depth 350 mm	350×150× 9× 6	Specimens with slab 500 × 100	3400	See Table 1	See Table 1

* D = depth of I-section; B = width of flange of I-section; t_f = thickness of flange of I-section; t_w = thickness of web of I-section.

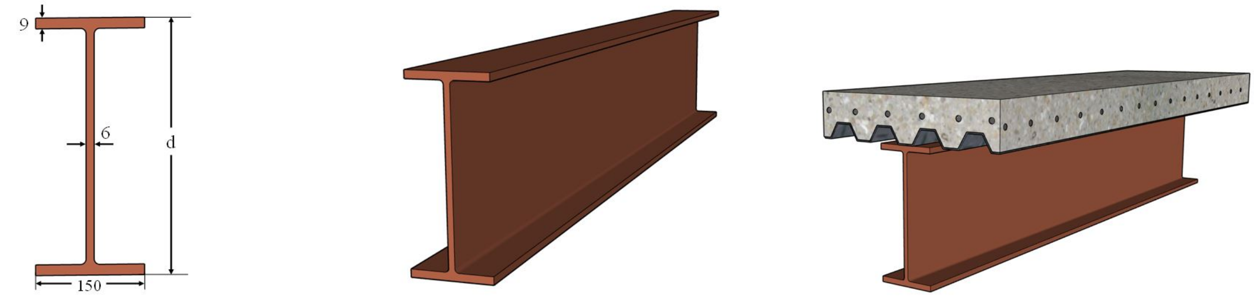

(a) Details of the free beam *(b) Unstrengthened beam without slab* *(c) Unstrengthened beam with slab*

Figure 11 Details of beams group 0.

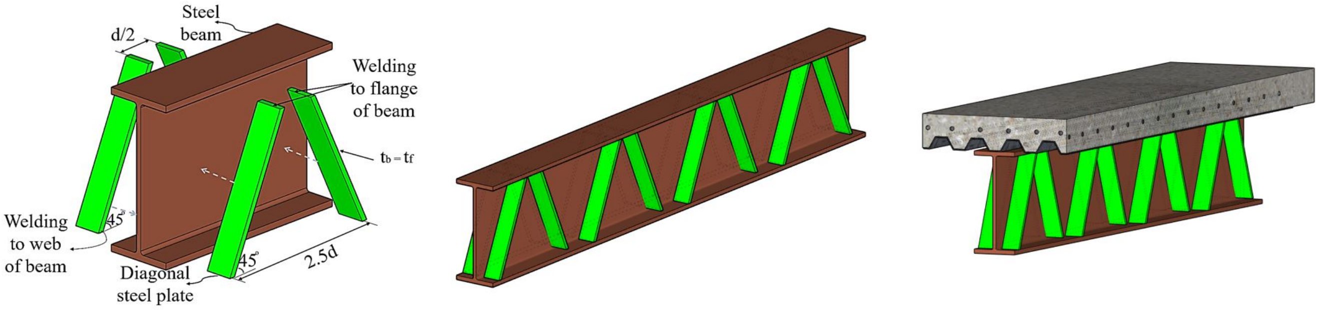

(a) Details of strengthening scheme-S1 *(b) Strengthened beam without slab* *(c) Strengthened beam with slab*

Figure 12 Details of strengthened beams group S1.

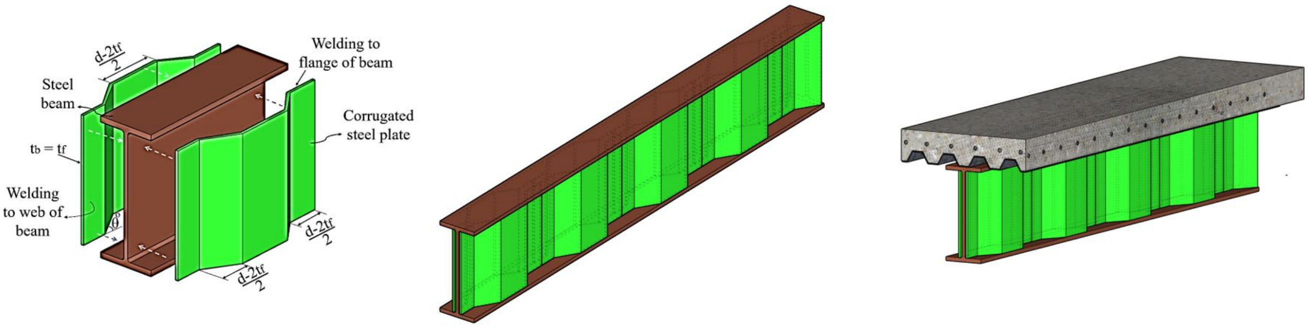

(a) Details of strengthening scheme-S2 *(b) Strengthened beam without slab* *(c) Strengthened beam with slab*

Figure 13 Details of strengthened beams group S2.

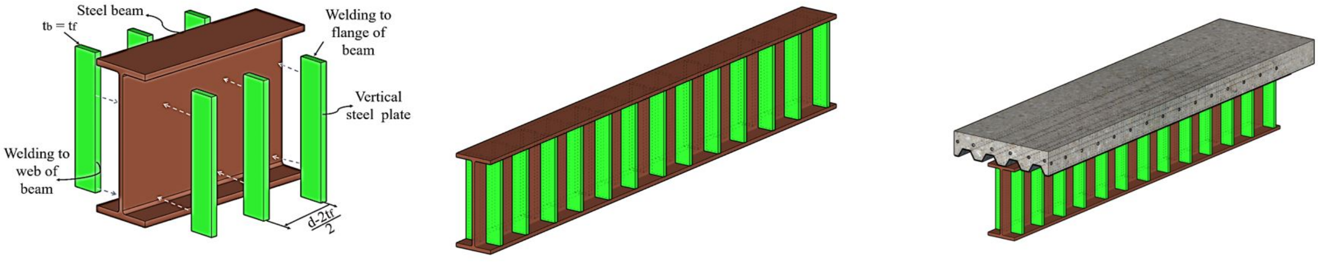

(a) Details of strengthening scheme-S3 *(b) Strengthened beam without slab* *(c) Strengthened beam with slab*

Figure 14 Details of strengthened beams group S3.

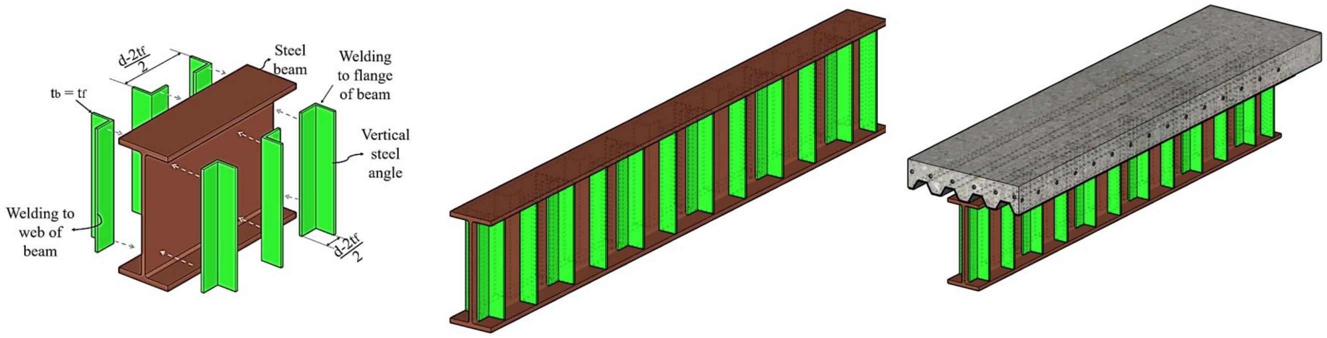

(a) Details of strengthening scheme-S4 *(b) Strengthened beam without slab* *(c) Strengthened beam with slab*

Figure 15 Details of strengthened beams group S4.

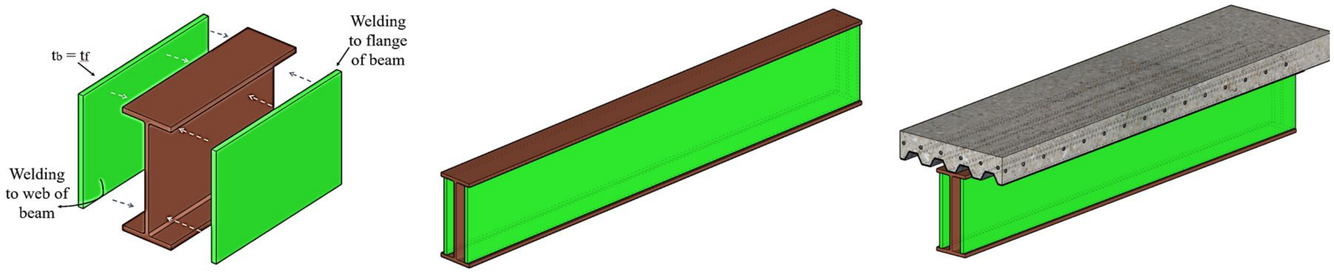

(a) Details of strengthening scheme-S5 *(b) Strengthened beam without slab* *(c) Strengthened beam with slab*

Figure 16 Details of strengthened beams group S5.

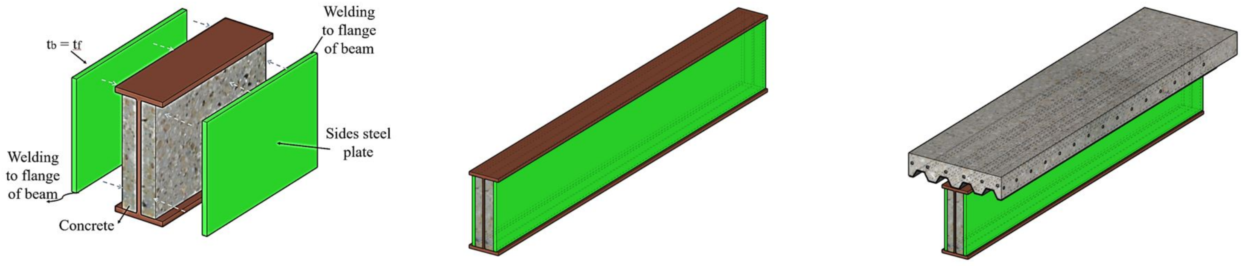

(a) Details of strengthening scheme-S6 *(b) Strengthened beam without slab* *(c) Strengthened beam with slab*

Figure 17 Details of strengthened beams group S6.

Table 5 FE parametric analysis for numerically studied steel I-beam.

Beam ID	Steel grade	Depth of beam (mm)	Composite floor slab
Group 0: Beams without strengthening (see Figure 11)			
A36-B-194-NS-C	A36	194	NO
A36-B-194-S-C	A36	194	YES
A36-B-350-NS-C	A36	350	NO
A36-B-350-S-C	A36	350	YES
A572-B-194-NS-C	A572	194	NO
A572-B-194-S-C	A572	194	YES
A572-B-350-NS-C	A572	350	NO
A572-B-350-S-C	A572	350	YES

Table 5 Continued...

Beam ID	Steel grade	Depth of beam (mm)	Composite floor slab
Group S1: Beams strengthened with diagonal stiffener plate welded to the web (see Figure 12)			
A36-B-194-NS-S1	A36	194	NO
A36-B-194-S-S1	A36	194	YES
A36-B-350-NS- S1	A36	350	NO
A36-B-350-S-S1	A36	350	YES
A572-B-194-NS-S1	A572	194	NO
A572-B-194-S-S1	A572	194	YES
A572-B-350-NS-S1	A572	350	NO
A572-B-350-S-S1	A572	350	YES
Group S2: Beams strengthened with corrugated plate welded to the web (see Figure 13)			
A36-B-194-NS-S2	A36	194	NO
A36-B-194-S-S2	A36	194	YES
A36-B-350-NS-S2	A36	350	NO
A36-B-350-S-S2	A36	350	YES
A572-B-194-NS-S2	A572	194	NO
A572-B-194-S-S2	A572	194	YES
A572-B-350-NS-S2	A572	350	NO
A572-B-350-S-S2	A572	350	YES
Group S3: Beams strengthened with vertical stiffener plates welded to the web (see Figure 14)			
A36-B-194-NS-S3	A36	194	NO
A36-B-194-S-S3	A36	194	YES
A36-B-350-NS-S3	A36	350	NO
A36-B-350-S-S3	A36	350	YES
A572-B-194-NS-S3	A572	194	NO
A572-B-194-S-S3	A572	194	YES
A572-B-350-NS-S3	A572	350	NO
A572-B-350-S-S3	A572	350	YES
Group S4: Beams strengthened with steel angle stiffener welded to the web (see Figure 15)			
A36-B-194-NS-S4	A36	194	NO
A36-B-194-S-S4	A36	194	YES
A36-B-350-NS-S4	A36	350	NO
A36-B-350-S-S4	A36	350	YES
A572-B-194-NS-S4	A572	194	NO
A572-B-194-S-S4	A572	194	YES
A572-B-350-NS-S4	A572	350	NO
A572-B-350-S-S4	A572	350	YES
Group S5: Beams strengthened with welded side plate along the inner side of the flanges (see Figure 16)			
A36-B-194-NS-S5	A36	194	NO
A36-B-194-S-S5	A36	194	YES
A36-B-350-NS-S5	A36	350	NO
A36-B-350-S- S5	A36	350	YES
A572-B-194-NS-S5	A572	194	NO
A572-B-194-S-S5	A572	194	YES
A572-B-350-NS-S5	A572	350	NO
A572-B-350-S-S5	A572	350	YES

Table 5 Continued...

Beam ID	Steel grade	Depth of beam (mm)	Composite floor slab
Group S6: Beams strengthened with partially encased-concrete along the web of beam (see Figure 17)			
A36-B-194-NS-S6	A36	194	NO
A36-B-194-S-S6	A36	194	YES
A36-B-350-NS-S6	A36	350	NO
A36-B-350-S- S6	A36	350	YES
A572-B-194-NS-S6	A572	194	NO
A572-B-194-S-S6	A572	194	YES
A572-B-350-NS-S6	A572	350	NO
A572-B-350-S-S6	A572	350	YES

3 FE RESULTS AND DISCUSSIONS

3.1 Modes of failure

According to the AISC (2016) code of practice for steel construction, lateral torsional buckling will not occur if the compression flange of a member is braced laterally or if twisting of the beam is prevented at frequent intervals. In all tests, three failure modes occurred: flexural failure (plastic behavior); inelastic buckling that occurs when the beam bends until the yield strain is reached in some, but not all, of its compression elements before lateral buckling; and lateral torsional buckling (elastic behavior) (see Figure 18–20). In order to demonstrate the FE modes of failure of the specimens, it was sufficient to demonstrate the modes of failure for all specimens of A36 steel in the FE test (Figure 18–20). As A36 and A572 were nearly identical in terms of the final failure shape, and because the total number of specimens for A36 and A572 was 56, it was enough to present the FE modes of failure for the A36 specimens with 194mm dipth, which included 20 specimens.

For control specimens (without slab) only, the beam buckled elastically before the yield stress reached anywhere. As the load on the control beam increased, the cross-section of the beam was twisted, and the compression flange was shifted laterally before reaching M_{p-uns} (plastic moment of the unstrengthened beam), as illustrated in Figure 18 (a) and (c). This failure occurred for all the control specimens without a slab, regardless of whether they were A36 or A572 type, and for depths of both 194 and 350 mm. A flexural failure was observed in control specimens made with slab for all A36 or A572 types, and for depths of 194 and 350 mm. Due to the slab resting on the top flange of the steel beam, we found that it loaded until its full plastic moment M_p was reached at some point or points of the steel beam; further loading then produced a redistribution of moments and concrete crushing, as shown in Figure 18 (b) and (d). In other words, due to the slab, the moments in these beams can reach M_p and then develop a rotation capacity sufficient for moment redistribution.

For strengthened specimens, all strengthening techniques were successful in increasing the steel beam's moment capacity to a level that was significantly higher than the full plastic moment of the unstrengthened beam (M_{p-uns}). Due to the different types of strengthening techniques, each technique's ability to increase the efficiency of the steel beam differed in terms of the resistance of the steel beam to external loads in comparison to its design capacity. The specimens without a slab and with A36 steel grade and a depth of 194 mm (A36-B-194-NS-S1, A36-B-194-NS-S3, and A36-B-194-NS-S4) had high stiffness at first until they reached more than full plastic moment of the unstrengthened beam (M_{p-uns}). Then, when the displacement reached approximately 85 mm, the beam experienced lateral torsional buckling, which was caused by the type and design of the strengthening techniques used (see Figure 19 (a), (c), (d)). On the other hand, for the same specimens, but with an increase in depth from 194 to 350 mm, there was an increase in resistance of the strengthened beams to longitudinal torsional buckling, indicating that the effect of depth in conjunction with the beam or the strengthening technique was large and effective.

Figure 19 (b) illustrates the final deformed shape and failure modes of the A36-B-194-NS-S2 specimen after it was strengthened with a corrugated steel plate welded to the steel I-beam's web. The deformed shape shown in Figure 19 (b) indicates that the beam's end began to bend. As illustrated in Figure 19 (b), the corrugated steel plate deformed at the web of the steel I-beam near the middle span, and the equivalent stress (moment and shear) developed at loaded points. This technique, S2, outperformed the S1, S3, and S4 techniques in terms of flexural stiffness and resistance to lateral torsional buckling. As illustrated in Figure 20 (b), the flexural stiffness and lateral torsional buckling resistance of the same specimen with slab (A36-B-194-S-S2) increased, and the failure was caused by concrete crushing and crack patterns.

The final failure mode for the A36-B-194-NS-S5 specimen is depicted in Figure 19 (d), which was strengthened with welded side plates along the inner side of the flanges on the inside of the specimen. It was found that S5 specimens made with or without slab for all A36 or A572 types and for depths of 194 and 350 mm failed due to flexural failure. All of this was possible because of the lateral strengthening that extended along the web of the beam, which increased the strength of the section. In comparison to its predecessors (S1, S3, S4), the performance of this strengthening technique (S5) was better because it demonstrated better performance, including lateral torsional buckling prevention and increasing the load capacity of the beam.

For the A36-B-194-NS-S6 specimen, which was similar to specimen A36-B-194-NS-S5 in terms of how it was strengthened, it was constructed using a different technique; this technique differed in that the space between the side plate and the web of the beam was filled with concrete, which increased the strength of the specimen and resulted in extremely good performance. Figures 18 (d) and 20 depict the type of failure, which was flexural with concrete crushing in the case of the specimens with slab.

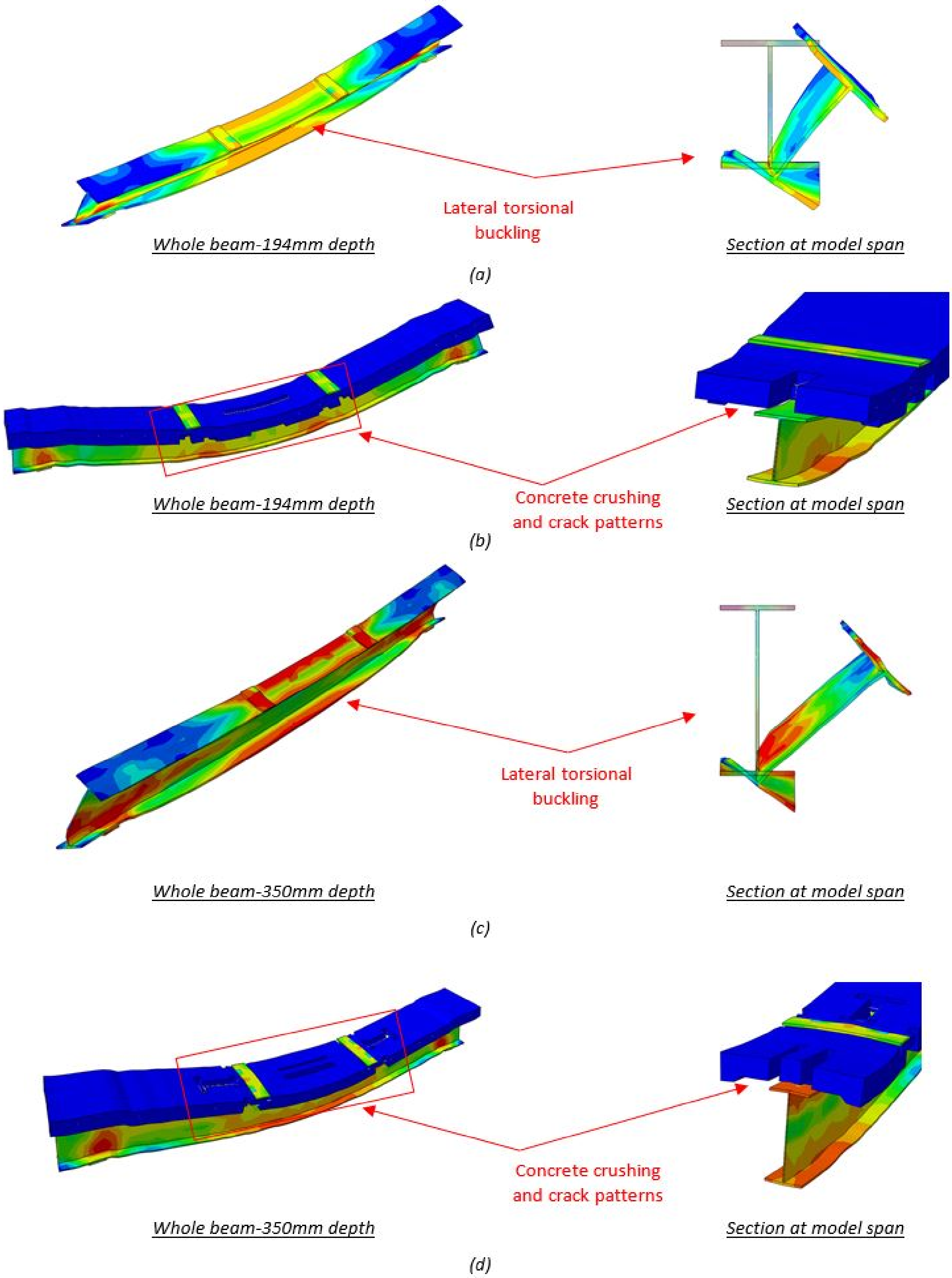

Figure 18 FE failure mode for numerically investigated Unstrengthened beam: (a) A36-B-194-NS-C; (b) A36-B-194-S-C; (c) A36-B-350-NS-C; (d) A36-B-350-S-C

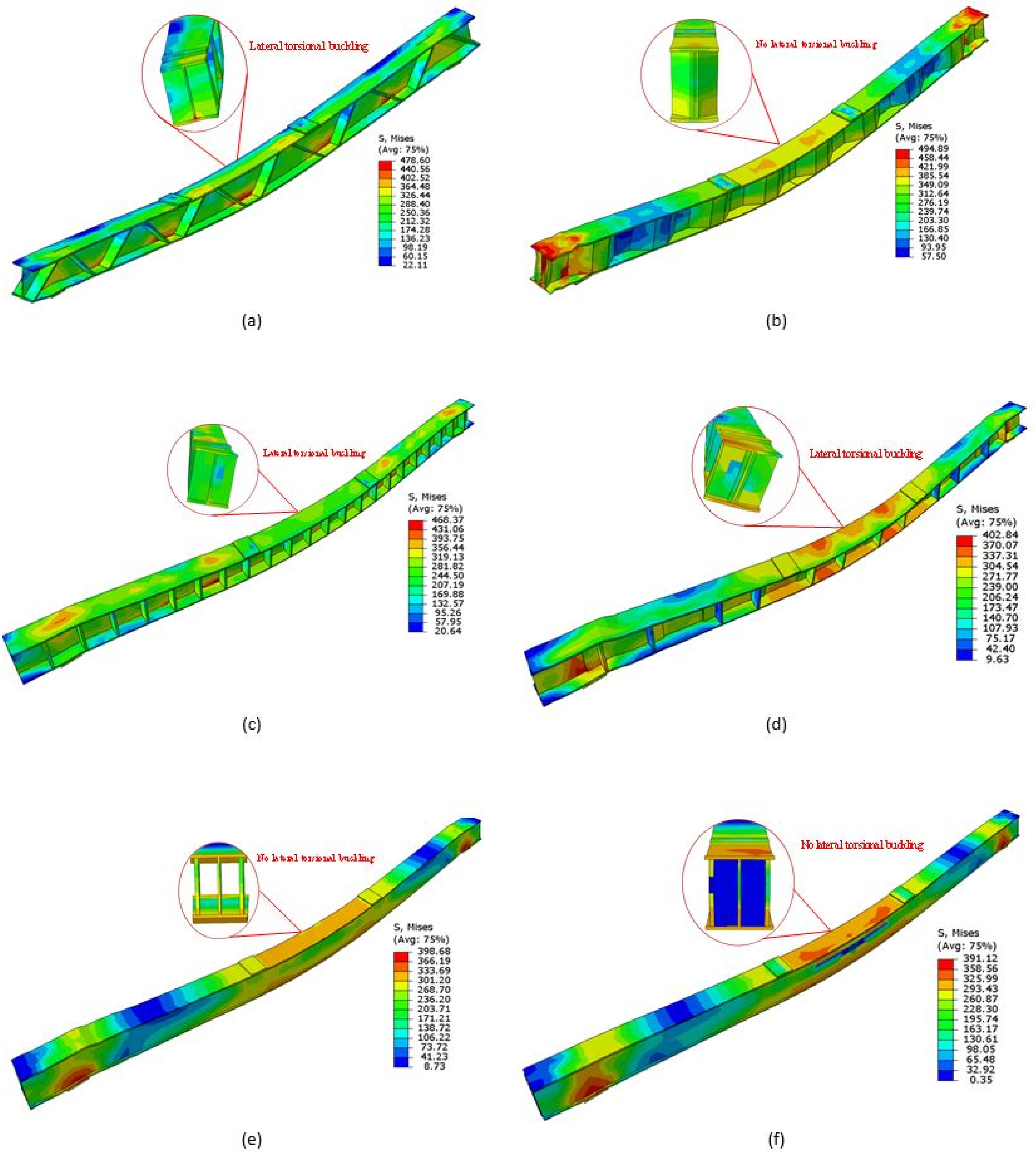

Figure 19 FE failure mode for numerically investigated strengthened beam: (a) A36-B-194-NS-S1; (b) A36-B-194-NS-S2; (c) A36-B-194-NS-S3; (d) A36-B-194-NS-S4; (d) A36-B-194-NS-S5; (d) A36-B-194-NS-S6.

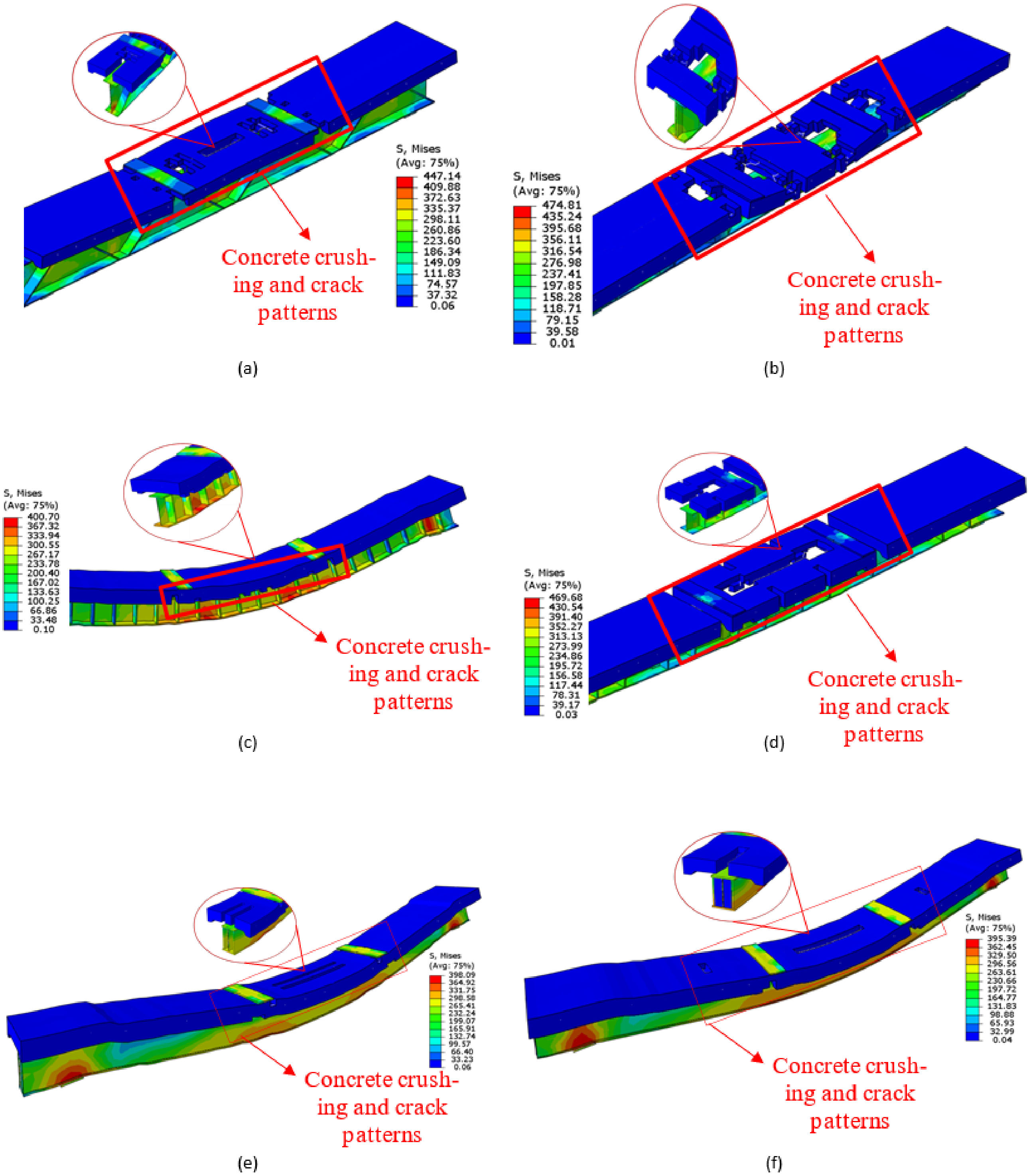

(a) (b) (c) (d) (e) (f)

Figure 20 FE failure mode for numerically investigated strengthened beam: (a) A36-B-194-S-S1; (b) A36-B-194-S-S2; (c) A36-B-350-S-S3; (d) A36-B-350-S-S4; (e) A36-B-350-S-S5; (f) A36-B-350-S-S6.

3.2 Load-displacement response

Figure 21 shows the load versus mid-span displacement for strengthening beams (A36 and 194 mm depth) without a slab in comparison to a control beam. Figures 22 shows the peak load capacity and energy dissipated for all FE specimens, while Figure 23 shows the moment capacity comparison. As well as Figures 24–27 show a comparison of load versus mid-span displacement curves for all FE specimens. Tables A1 and A2 summarize the test results for 56 specimens in terms of load-displacement curve parameters.

For strengthened specimens A36-B-194-NS-S1, A36-B-194-NS-S3, and A36-B-194-NS-S4, and as indicated in Figure 21 (a), (c), (d), their behavior was nearly identical. The specimens were in the elastic range during the initial loading stage, and the applied load increased almost linearly due to the stiff section and strengthening techniques. The yielding of the beam's flange occurred at mid-span displacements of 7.34 mm, 7.48 mm, and 7.57 mm for A36-B-194-NS-S1, A36-B-194-NS-S3, and A36-B-194-NS-S4, respectively, with applied load of 165.34 kN, 171.61 kN, and 206.87 kN. After yielding started, the second stage was initiated, and the flexural stiffness began to decrease. For A36-B-194-NS-S1, A36-B-194-NS- S3, and A36-B-194-NS- S4, the maximum applied force was 239.19 kN, 244.98 kN, and 288.28 kN, respectively, and the corresponding mid-span displacement was 60.71 mm, 70.16 mm, and 80 mm. Lateral torsional buckling began at the mid-span displacement (86.20 mm, 87.92 mm, and 84.75 mm for A36-B-194-NS-S1, A36-B-194-NS-S3, and A36-B-194-NS-S4, respectively).This lateral torsional buckling was associated with a significant decrease in applied force (see Figure 21 (a), (c), (d)). Figure 21(b) illustrates the load versus mid-span displacement curve for strengthened specimen A36-B-194-NS-S2 which was strengthened using a corrugated steel plate welded to the web of the beam.

The beam remained in the elastic stage up to approximately 8.35 mm displacement, and until approximately 52.98 mm displacement, the beam's performance was dominated by flexure. The corresponding peak load was 471.52 kN at 52.98 mm mid-span displacement. As a result, the steel beam and welded corrugated plates were deformed. Figure 21 (e) and (f) show the load versus mid-span displacement curves for strengthened specimens A36-B-194-NS-S5 and A36-B-194-NS-S6. The difference between A36-B-194-NS-S5 and A36-B-194-NS-S6 was that the space between the side steel plate and the web of the beam was filled with concrete for A36-B-194-NS-S6, which made a significant difference in terms of stiffness and maximum load. At first, both specimens' curves were stiff; the yielding of A36-B-194-NS-S5 and A36-B-194-NS-S6 was at displacements of 8.15 mm and 7.66 mm, respectively, with corresponding loads of 342.62 kN and 380.79 kN. The maximum applied force in the pure flexural stage was 447.07 kN and 520.98 kN for A36-B-194-NS-S5 and A36-B-194-NS-S6, respectively, with corresponding vertical displacements of 31.81 mm and 20.62 mm.

It should be noted that the results presented in Figures 21–23 are limited to the A36 specimens with a depth of 194 mm and without the slab. They are presented to illustrate the difference between an unstrengthened beam and a strengthened beam, as well as how to apply each technique in the presence of load and displacement. Whereas in Figures 24–27, all specimens are presented in terms of load and displacement, as are all results in appendix A (Tables A1 and A2).

The peak load capacity and energy dissipated as shown in Figure 22, as well as the moment capacity comparison shown in Figure 23, demonstrating that strengthened specimens A36-B-194-NS-S1, A36-B-194-NS-S3, and A36-B-194-NS-S4 performed exceptionally well in comparison to the unstrengthened beam C. The peak load that specimens A36-B-194-NS-S1, A36-B-194-NS-S3, and A36-B-194-NS-S4 resisted was approximately 1.60, 1.63, and 1.91 times that of unstrengthened beam C. Furthermore, as shown in Table A1, the displacement and energy ductility ratios of specimens A36-B-194-NS-S1, A36-B-194-NS-S3, and A36-B-194-NS-S4 were extremely high in comparison to the unstrengthened beam C. As illustrated in Figure 23, the moment capacity of unstrengthened beam C was extremely low, indicating their high susceptibility to lateral torsional buckling, in contrast to strengthened beams whose moment capacity was increased to the full plastic moment, where the moment capacity ratios compared with $M_{p\text{-}uns}$ (plastic moment of the unstrengthened beam) were 1.47, 1.50, and 1.77 times those of specimens A36-B-194-NS-S1, A36-B-194-NS-S3, and A36-B-194-NS-S4, respectively. The ultimate load that strengthened specimens A36-B-194-NS-S2, A36-B-194-NS-S5, and A36-B-194-NS-S6 were able to resist was approximately 3.13, 2.97, and 3.46 times that of the unstrengthened beam C, respectively. Additionally, the energy dissipated was significantly increased as a result of strengthening techniques for A36-B-194-NS-S2, A36-B-194-NS-S5, and A36-B-194-NS-S6. The moment capacity of specimens A36-B-194-NS-S2, A36-B-194-NS-S5, and A36-B-194-NS-S6 at their ultimate state was approximately 2.90, 2.75, and 3.20 times that of unstrengthened beam C. It is obvious that the sixth strengthened specimen, A36-B-194-NS-S6, carried a significantly greater load than the other specimens. Figures 24-28 show a comparison of the peak load and moment capacity of all tested beams at their ultimate state. The S6, S2, and S5 techniques had the highest peak load and moment capacities of all the beams tested. In the beams, it was discovered that strengthening existing steel I-beams using strengthening techniques (S1, S3, and S4) was effective in increasing the peak load of specimens during four-point bending tests when the beam's depth was increased and the material type was changed. Additionally, the total energy dissipated in the ultimate state also increased as a result of strengthening techniques (S1, S3, and S4).

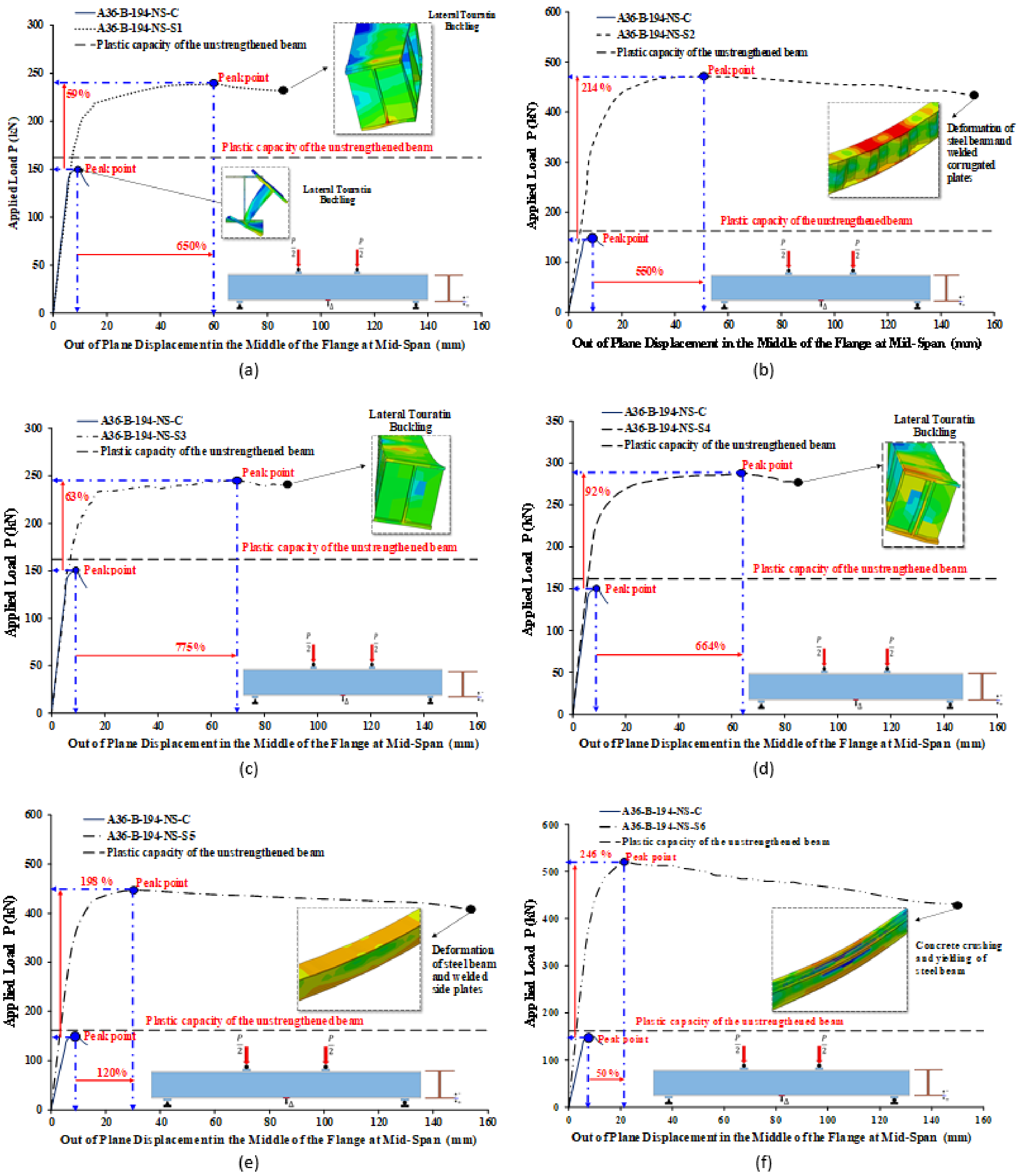

Figure 21 FE load-displacement curves for strengthening beams (A36-194) without slab compared to control beam: (a) A36-B-194-NS-S1; (b) A36-B-194-NS-S2; (c) A36-B-194- NS-S3; (d) A36-B-194- NS-S4; (e) A36-B-194- NS-S5; (f) A36-B-194- NS-S6.

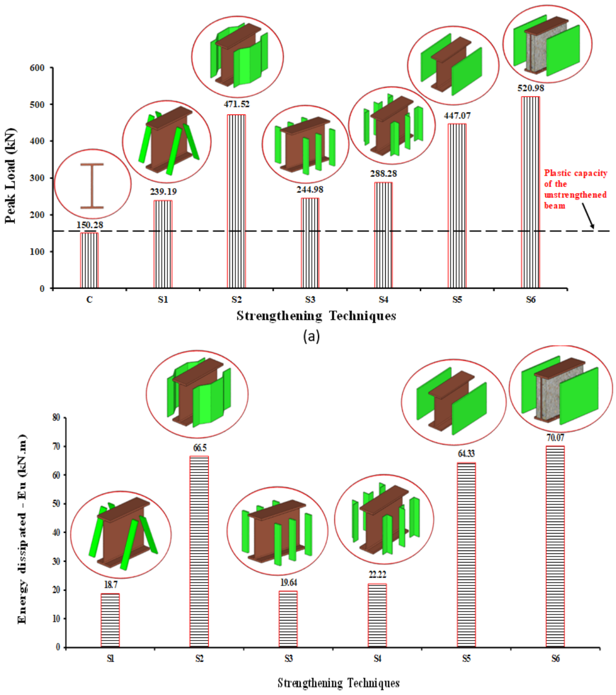

Figure 22 Comparison of all types of strengthening techniques in terms of: (a) Peak load capacity; (b) Energy dissipated.

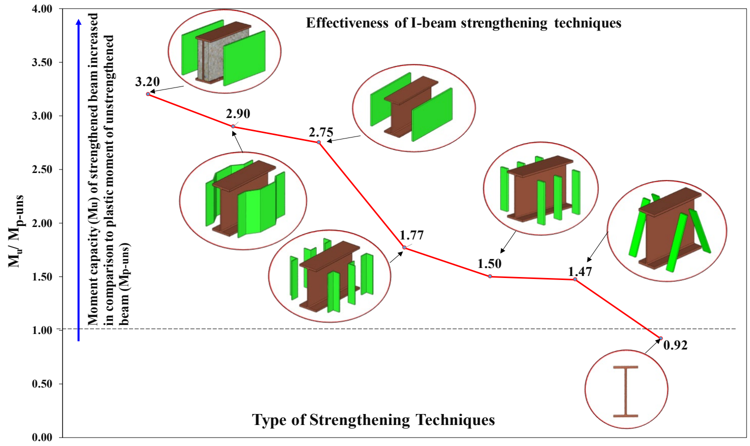

Figure 23 Comparison of the effectiveness of steel I-beam strengthening techniques in terms of moment capacity compared to the plastic moment of the unstrengthened beam ($M_{p\text{-}uns}$).

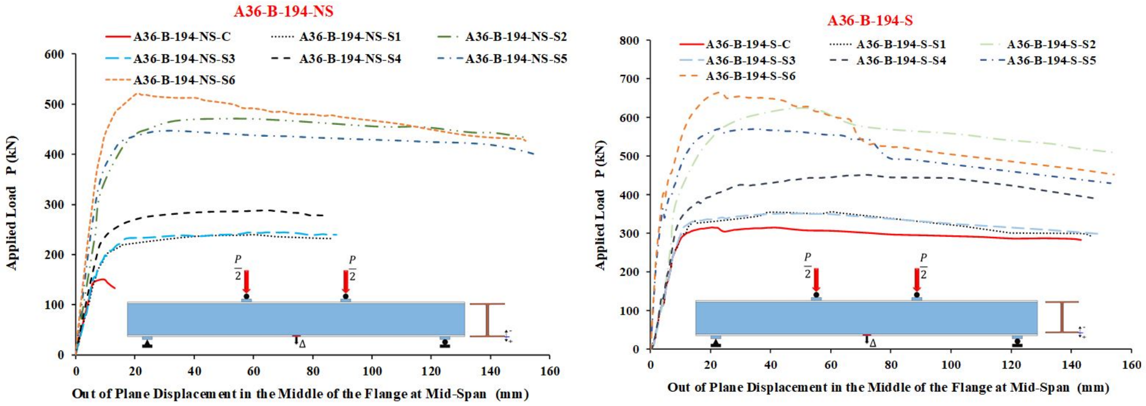

*(**a**) Beams without slab and 194 mm depth* *(**b**) Beams with slab and 194 mm depth*

Figure 24 FE load-displacement curves for strengthening beams for steel grade A36 and the depth of beam is 194 mm.

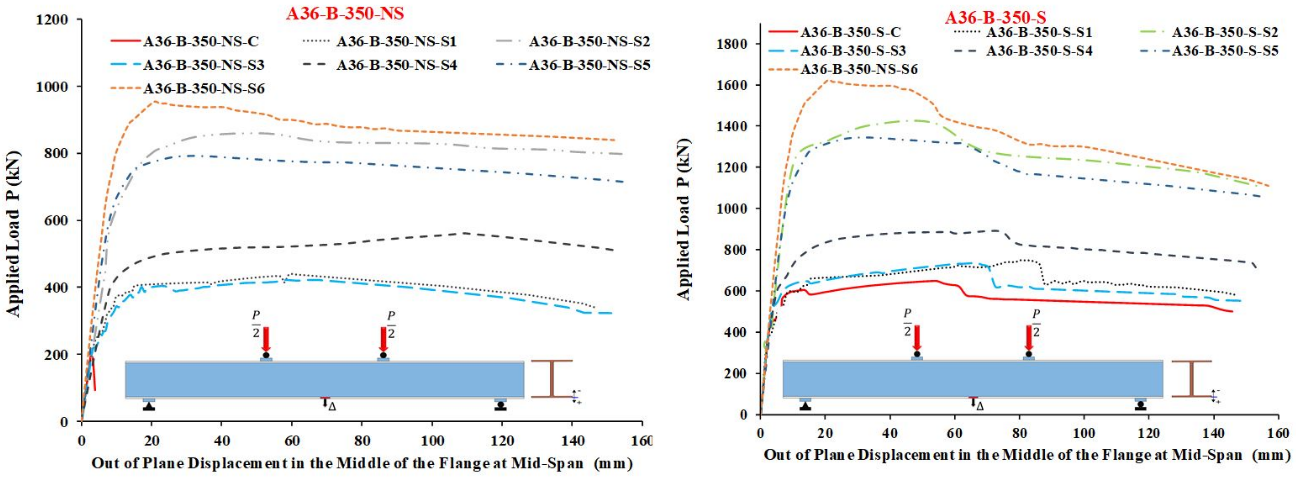

(a) Beams without slab and 350 mm depth

(b) Beams with slab and 350 mm depth

Figure 25 FE load-displacement curves for strengthening beams for Steel grade A36 and the depth of beam is 350 mm.

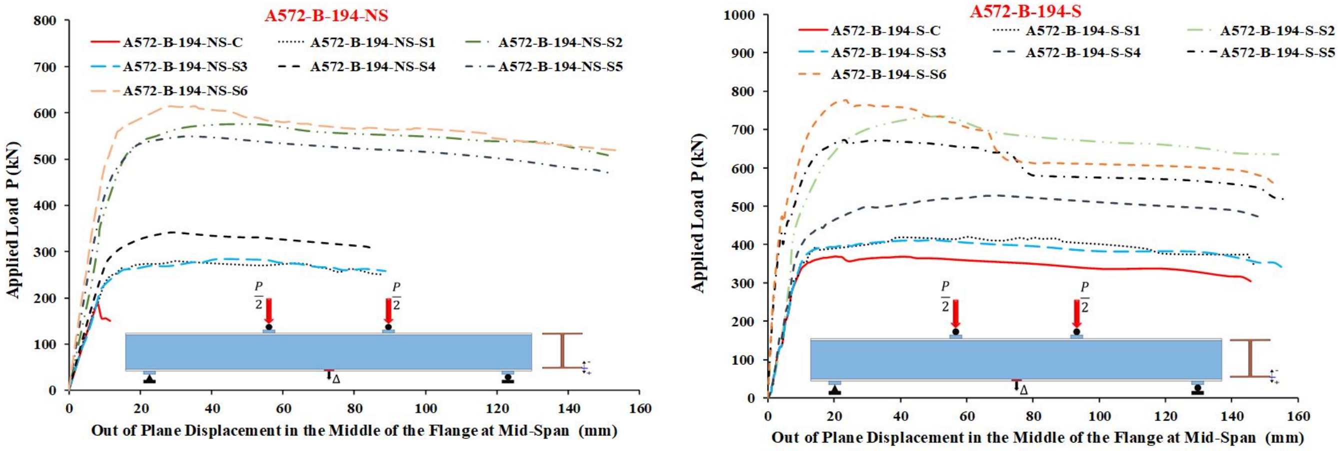

(a) Beams without slab and 194 mm depth

(b) Beams with slab and 194 mm depth

Figure 26 FE load-displacement curves for strengthening beams for Steel grade A572 and the depth of beam is 194 mm.

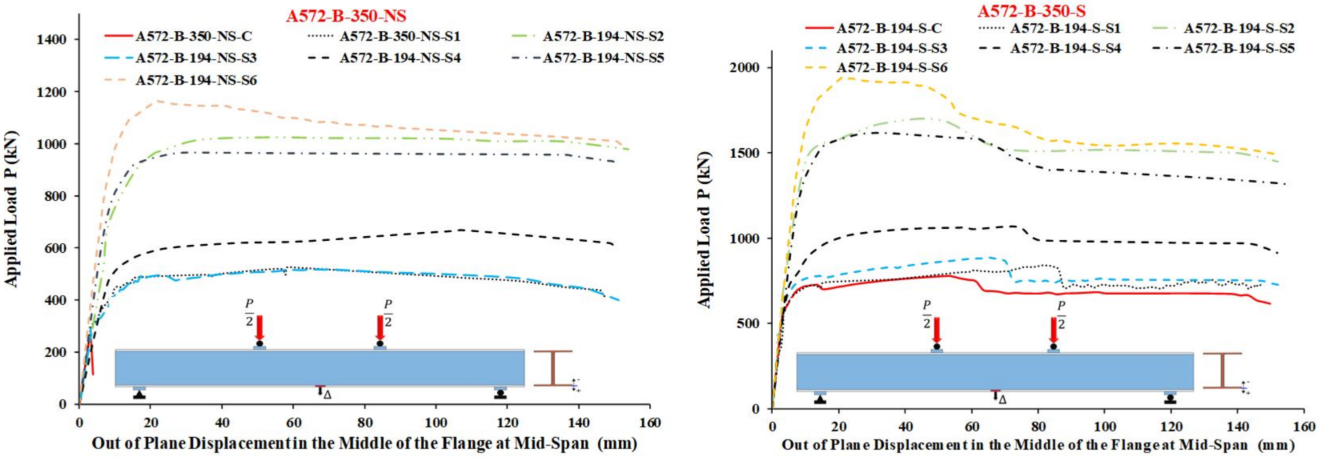

(a) Beams without slab and 350 mm depth

(b) Beams with slab and 350 mm depth

Figure 27 FE load-displacement curves for strengthening beams for steel grade A572 and the depth of beam is 350 mm.

4 EFFECT OF PARAMETRIC STUDY

Comparing specimens with A36 or A572, all specimens with A572 had efficient load-displacement characteristics. It should be noted that the increase between the A36 and the A572 was approximately 19% on average. On the other hand, the difference in depth between specimens with a depth of 194 mm and those with a depth of 350 mm was approximately 79%. It is apparent from this research that when the depth of the steel I-beam section is increased, the dimensions and details of the strengthening methods are enhanced, resulting in a rise in the efficacy of the strengthening techniques. As previously stated, the design of strengthening techniques is primarily determined by the dimensions of the beam section. When comparing specimens with composite floor slabs to specimens without composite floor slabs, the increase was approximately 38%.

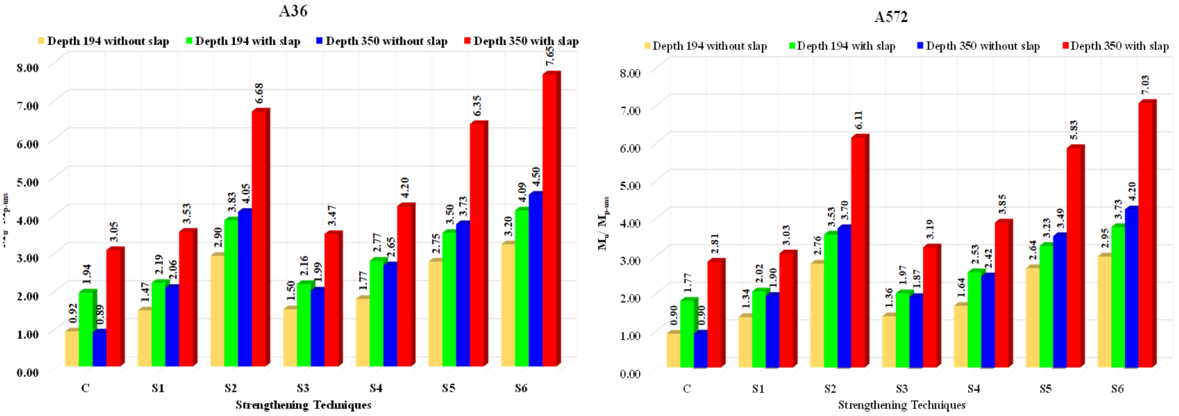

(a) *Steel grade A36* (b) *Steel grade A572*

Figure 28 Moment capacity (M_u) comparison of all types of strengthening techniques compared to the plastic moment of the unstrengthened beam (M_{p-uns}) for steel grade A36 and A572 in the case of: depth of beam is 194 mm with and without slab, depth of beam is 350 mm with and without slab.

5 COST ANALYSIS FOR STRENGTHENING TECHNIQUES

Independent of the findings regarding the efficacy of the studied strengthening techniques, the selection of a strengthening technique should always be guided by an evaluation of the intervention cost in relation to the expected behavior, with the goal of maximizing the behavior while keeping application costs to an absolute minimum. The costs of applying strengthening techniques were calculated based on the values shown in Table 6. On the basis of local material and labor costs, average values were also used in this study. An absolute analysis was used in this work to evaluate the cost relationship of strengthening techniques. This analysis considered the increase in load-bearing capacity of each technique, relative to the unstrengthened beam, in relation to the cost of the intervention (Figure 29).

Table 6. Cost of application of the strengthening schemes. *

Strengthening technique	Material cost ($)							Welding / cutting / cost ($)	Technical labor, supervision, machinery/ cost ($/hour)	Total cost ($)	Increase in cost (%)
	Steel I-Beam	Diagonal steel plate stiffener	Corrugated steel plate	Vertical steel plate stiffener	Steel angle stiffener	Side steel plate	Concrete				
C	120	-	-	-	-	-	-	-	-	120	-
S1	120	34	-	-	-	-	-	32	40	226	90
S2	120	-	70	-	-	-	-	45	60	294	146
S3	120	-	-	34		-	-	60	40	253	112
S4	120	-	-	-	37	-	-	65	45	267	123
S5	120	-	-	-	-	65	-	40	40	264	121
S6	120	-	-	-	-	65	8	40	70	342	186

*The pricing was based on local material and labor costs.

It should be noted that the increased load-bearing capacity of each strengthened beam does not always imply an increase in cost. To calculate the effectiveness of each technique used for upgrading steel I-beams, a percentage of load-bearing capacity and cost should be used so that they can be easily compared. As a result, it was decided to use an easy-to-use method for both the practical and research sides, as it provides an indication of which techniques are better and more efficient in terms of performance and cost. The unstrengthened beam was used as a reference specimen in terms of load-bearing capacity and cost, and all strengthened beams were compared to it. When calculating the effectiveness of each technique, the computed costs are divided by the load-bearing capacity of each technique and then subtracted from the unstrengthened beam to arrive at a percentage of the cost of each technique. Each specimen had two characteristics: load-bearing capacity and cost. If the percentage of the cost of the strengthened beam versus the cost of the unstrengthened beam is greater than the percentage of increase in the load-bearing capacity of the strengthened beam versus the unstrengthened beam, the technique is ineffective, and vice versa. Figure 29 illustrates the overall trend in the percentage increase in cost in relation to the percentage increase in load-bearing capacity, from the least expensive to the most expensive technique. However, there were some exceptions, such as the situations in which beams were strengthened (S2, S5, and S6) typically resulting in the greatest increase in load-bearing capacity, as opposed to the S1, S3, and S4 techniques. While these graphs are useful in assessing the absolute behavior of the selected strengthening techniques, they do not represent the most economical or effective method of selecting the type of strengthening technique and rely on it to increase the beam's efficiency. As illustrated in Figure 30, it was necessary to describe the selection of the most cost-effective and economical strengthening technique by comparing the percentage increase in load-bearing capacity caused by the strengthening technique to the cost of the strengthening technique and determining whether the technique is feasible or not.

After analyzing the cost and its relationship to the increase in the beam's efficiency through the use of different techniques, it was determined that the fifth type (S5) and the second type (S2) were the most cost-effective in terms of load-bearing capacity, followed by the sixth type (S6). Concerning the first technique type (S1), as well as the third (S3) and fourth (S4) techniques, it was determined that they were economically ineffective in terms of increasing the beam's efficiency (see Figure 30).

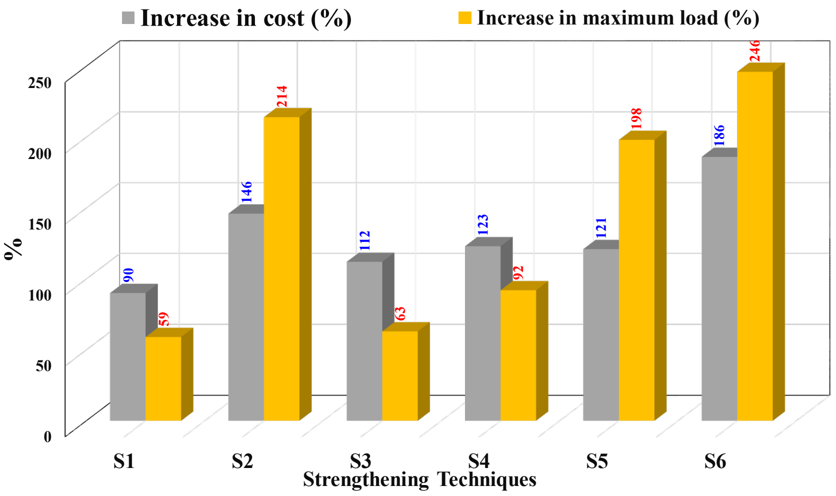

Figure 29 Comparison of cost increase and load gain as a result of strengthening.

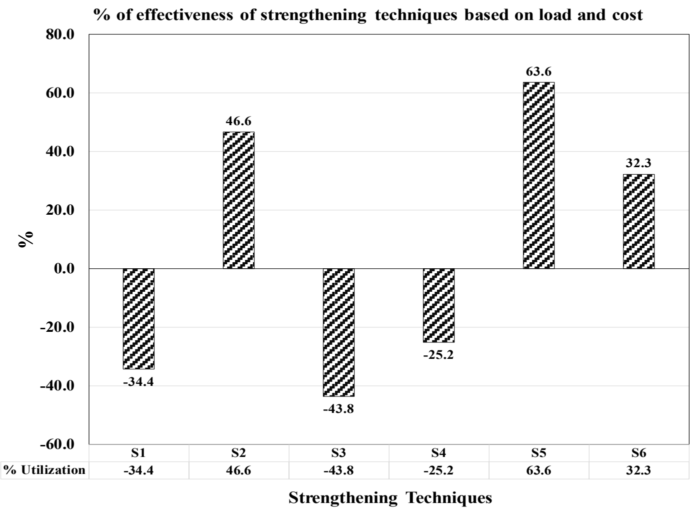

	S1	S2	S3	S4	S5	S6
% Utilization	-34.4	46.6	-43.8	-25.2	63.6	32.3

Figure 30 *Comparison of the effectiveness of strengthening techniques based on load and cost.*

6 CONCLUSIONS

The following are the main findings drawn from this research:

- Although the ultimate load and energy dissipated in all strengthened specimens were significantly greater than those in the existing unstrengthened beam C, they varied considerably. The peak load that specimens S1, S3, and S4 could withstand was approximately 1.60, 1.63, and 1.91 times that of unstrengthened beam C, respectively. The ultimate load that strengthened specimens S2, S5, and S6 could withstand was approximately 3.13, 2.97, and 3.46 times that of the unstrengthened beam C.
- Steel I-beam strengthening techniques (S2, S5, and S6) were found to significantly improve load-displacement characteristics in a four-point bending test. The moment capacity of the strengthened beams (S2, S5, and S6) increased significantly as a result of these techniques, by 215%, 200%, and 248%, respectively, when compared to the plastic moment of the unstrengthened beam.
- Among all the FE tested specimens, the S6 specimen, which was strengthened using welded side plates and partially encased concrete along the web of a beam, had the best performance in load-displacement characteristics under a four-point bending test.
- The use of A572 steel for steel beams and strengthening techniques and materials improved the load-displacement characteristics by approximately 19% when compared to A36 steel. On the other hand, the difference in depth between specimens with a depth of 194 mm and those with a depth of 350 mm was approximately 79%. When comparing specimens with composite floor slabs to specimens without composite floor slabs, the increase was approximately 38%.
- The cost versus efficiency analysis resulted in conclusions about the viability of implementing each strengthening technique, based on computed behavior and intervention costs. After analyzing the cost and its relationship to the increase in the beam's efficiency through the use of different techniques, it was determined that the fifth type (S5) and the second type (S2) were the most cost-effective in terms of load-bearing capacity, followed by the sixth type (S6). Concerning the first technique type (S1), as well as the third (S3) and fourth (S4) techniques, it was determined that they were economically ineffective in terms of increasing the beam's efficiency.

Acknowledgments

The author extends his appreciation to the Deanship of Scientific Research at Princess Nourah bint Abdulrahman University through the Fast-track Research Funding Program for funding the work and their technical support.

Editor: Marco L. Bittencourt.

References

Abaqus 6.20 Analysis User’s Guide, Section 12.9.3. (2020). Defining damages, Dassault Systemes Simulia Corp., Providence, RI, 2020.

Abaqus 6.20. (2020). Dassault Systèmes Simulia Corp.: Providence, RI (2020).

Al-Ridha, A. S., Atshan, A. F., Mahmoud, K. S., & Hameed, Q. K. (2019). Effect of strengthening of steel beams with variable length by using carbon fiber. Journal of Engineering, 2019.

Al-Saidy, A. H., Klaiber, F. W., & Wipf, T. J. (2004). Repair of steel composite beams with carbon fiber-reinforced polymer plates. Journal of Composites for Construction, 8(2), 163-172.

ANSI/AISC 360-16. (2016). Specifications for structural steel buildings. American Institute of Steel Construction, Chicago, IL, USA.

ASTM. (2014). Standard specification for high-strength steel bolts, Classes 10.9 and 10.9.3, for structural steel joints (Metric). ASTM A490M-14, American Society for Testing and Materials, West Conshohocken, PA, USA.

Chi, Y., Xu, L., & Yu, H. S. (2014). Plasticity model for hybrid fiber-reinforced concrete under true triaxial compression. Journal of Engineering Mechanics, 140(2), 393-405.

CEN. (1993). EN 10034: 1993–Structural steel I and H sections—Tolerances on shape and dimensions.

CEN, prEN 1993-1-14:2020-Eurocode 3: Design of Steel Structures — Part 1-14: Design Assisted by Finite Element Analysis, 2020. Brussels.

Dibley, J. E., BISRA, & BSC. (1969). LATERAL TORSIONAL BUCKLING OF I-SECTIONS IN GRADE 55 STEEL. Proceedings of the Institution of Civil Engineers, 43(4), 599-627.

Dinu, F., Marginean, I., & Dubina, D. (2017). Experimental testing and numerical modelling of steel moment-frame connections under column loss. Engineering Structures, 151, 861-878.

European Convention for Constructional Steelwork (ECCS) (1984). Ultimate limit state calculation of sway frames with rigid joints, Technical Committee 8–Structural Stability Technical Working Group, Publication No. 33, Brussels, Belgium, 1984

Feng, R., Zhan, H., Meng, S., & Zhu, J. (2018). Experiments on H-shaped high-strength steel beams with perforated web. Engineering Structures, 177, 374-394.

H.Y. Ban, M.A. Bradford, B. Uy, X. Liu. (2016). Available rotation capacity of composite beams with high-strength materials under sagging moment, J. Constr. Steel Res. 118 (3) 156–168.

Kabir, M. I., Lee, C. K., & Zhang, Y. X. (2021). Numerical and analytical investigations of flexural behaviours of ECC–LWC encased steel beams. Engineering Structures, 239, 112356.

Kabir, M. I., Lee, C. K., Rana, M. M., & Zhang, Y. X. (2020). Flexural behaviour of ECC-LWC encased slender high strength steel composite beams. Journal of Constructional Steel Research, 173, 106253.

Katwal, U., Tao, Z., & Hassan, M. K. (2018). Finite element modelling of steel-concrete composite beams with profiled steel sheeting. Journal of Constructional Steel Research, 146, 1-15.

Lakavath, C., Prakash, S. S., & Dirar, S. (2021). Experimental and numerical studies on shear behaviour of macro-synthetic fibre reinforced prestressed concrete beams. Construction and Building Materials, 291, 123313.

Lee, J., & Fenves, G. L. (1998). Plastic-damage model for cyclic loading of concrete structures. Journal of engineering mechanics, 124(8), 892-900.

Liu, Y., & Gannon, L. (2009). Experimental behavior and strength of steel beams strengthened while under load. Journal of Constructional Steel Research, 65(6), 1346-1354.

Lubliner, J., Oliver, J., Oller, S., & Onate, E. (1989). A plastic-damage model for concrete. International Journal of solids and structures, 25(3), 299-326.

Nozaka, K., Shield, C. K., & Hajjar, J. F. (2005). Effective bond length of carbon-fiber-reinforced polymer strips bonded to fatigued steel bridge I-girders. Journal of Bridge Engineering, 10(2), 195-205.

Rossi, A., Nicoletti, R. S., de Souza, A. S. C., & Martins, C. H. (2020). Numerical assessment of lateral distortional buckling in steel-concrete composite beams. Journal of Constructional Steel Research, 172, 106192.

Sayed-Ahmed, E. Y. (2006). Numerical investigation into strengthening steel I-section beams using CFRP strips. In Structures Congress 2006: Structural Engineering and Public Safety (pp. 1-8).

Sen, R., Liby, L., & Mullins, G. (2001). Strengthening steel bridge sections using CFRP laminates. Composites Part B: Engineering, 32(4), 309-322.

S. Shayan, K.J.R. Rasmussen, H. Zhang, (2012). On the modelling of initial geometric imperfections and residual stress of steel frames, Research Report R935, School of Civil Engineering, The University of Sydney, Sydney, Australia.

Timoshenko, S. P., & Gere, J. M. (2009). Theory of elastic stability. Courier Corporation.

Yan, S., Zhao, X., & Wu, A. (2018). Ductile fracture simulation of constructional steels based on yield-to-fracture stress–strain relationship and micromechanism-based fracture criterion. Journal of Structural Engineering, 144(3), 04018004.

Yossef, N. M. (2015). Strengthening Steel I-Beams by Welding Steel Plates before or While Loading. International Journal of Engineering Research & Technology (IJERT), 4(07).

Yu, T., Teng, J. G., Wong, Y. L., & Dong, S. L. (2010). Finite element modeling of confined concrete-II: Plastic-damage model. Engineering structures, 32(3), 680-691.

Appendix A

Table A1 FE results for steel I-beams for all A36 specimens.[1]

Beam ID	P_y (kN)	Ä$_y$ (mm)	P_u (kN)	Ä$_{u,k}$ (mm)	M_u (kN.m)	M_p (kN.m)	M_u/ $M_{p\text{-}uns*}$	K_s (kN/mm)	Ä$_u$ (mm)	ì$_Ä$	E_u (kN·m)
A36-Beams without slab and 194 mm depth											
A36-B-194-NS-C	-	-	150.28	9.36	76.64	82.8*	0.92	-	9.36	-	-
A36-B-194-NS-S1	165.34	7.34	239.19	60.71	121.89	132.4	1.47	22525	86.20	11.47	18.70
A36-B-194-NS-S2	322.23	8.35	471.52	52.98	240.47	243.6	2.90	38590	152.60	18.27	66.50
A36-B-194-NS-S3	171.61	7.48	244.98	70.16	124.93	133.8	1.50	22942	87.92	11.75	19.64
A36-B-194-NS-S4	206.87	7.57	288.28	81.00	146.64	152.5	1.77	27327	84.75	11.19	22.22
A36-B-194-NS-S5	342.62	8.15	447.07	31.81	228.0	233.3	2.75	42039	150.44	18.94	64.33
A36-B-194-NS-S6	380.79	7.66	520.98	20.62	265.69	269.6	3.20	49711	151.89	19.82	70.07
A36-Beams with slab and 194 mm depth											
A36-B-194-S-C	286.31	10.06	315.05	20.42	160.67	163.2	1.94	28460	143.28	14.24	41.33
A36-B-194-S-S1	298.76	10.32	355.87	60.71	181.49	186.5	2.19	28949	150.18	14.55	46.50
A36-B-194-S-S2	377.20	8.35	623.15	52.98	317.81	324.7	3.83	45173	154.26	18.47	82.55
A36-B-194-S-S3	313.60	10.83	351.37	50.64	179.19	180.6	2.16	28956	149.05	13.78	47.47
A36-B-194-S-S4	327.41	9.36	450.39	69.74	229.79	232.4	2.77	34979	148.53	15.86	60.72
A36-B-194-S-S5	446.90	8.85	569.59	35.06	290.49	293.1	3.50	50497	153.06	17.29	75.72
A36-B-194-S-S6	497.79	8.43	664.26	22.74	338.77	340.1	4.09	59049	154.22	18.29	82.90
A36-Beams without slab and 350 mm depth											
A36-B-350-NS-C	-	-	188.47	3.22	96.12	108*	0.89	-	3.22	-	-
A36-B-350-NS-S1	319.83	7.34	437.94	59.21	223.34	226.5	2.06	43573	147.18	20.05	57.75
A36-B-350-NS-S2	386.72	5.88	858.17	52.90	437.66	439.6	4.05	65768	154.03	26.19	121.52
A36-B-350-NS-S3	245.77	5.30	421.53	67.16	214.98	217.5	1.99	46371	151.14	28.51	56.90
A36-B-350-NS-S4	376.50	7.57	561.91	109.12	286.57	290.6	2.65	49735	151.91	20.06	77.28
A36-B-350-NS-S5	452.64	5.52	791.31	31.81	403.56	409.1	3.73	82000	154.44	27.97	113.37
A36-B-350-NS-S6	629.72	6.63	953.41	20.62	486.23	490.5	4.50	94980	151.89	22.90	130.10

Table A1 Continued...

Beam ID	P_y (kN)	$Ä_y$ (mm)	P_u (kN)	$Ä_{u,k}$ (mm)	M_u (kN.m)	M_p (kN.m)	M_u/ $M_{p\text{-uns*}}$	K_s (kN/mm)	$Ä_u$ (mm)	$ì_Ä$	E_u (kN·m)
A36-Beams with slab and 350 mm depth											
A36-B-350-S-C	488.79	5.92	647.85	54.48	330.40	333.2	3.05	82565	145.74	24.61	82.40
A36-B-350-S-S1	510.08	5.34	748.49	80.21	381.73	384.0	3.53	95520	150.18	28.12	97.00
A36-B-350-S-S2	586.45	4.35	1415.95	52.93	722.13	726.1	6.68	134816	154.03	35.50	189.48
A36-B-350-S-S3	547.50	5.17	736.71	66.39	375.72	378.2	3.47	105899	150.39	29.08	94.16
A36-B-350-S-S4	599.78	5.02	890.22	73.49	454.01	459.9	4.20	119478	153.03	30.48	122.54
A36-B-350-S-S5	769.49	5.52	1345.01	30.80	685.95	688.7	6.35	139400	154.44	27.91	180.86
A36-B-350-S-S6	923.40	5.68	1620.80	20.62	826.60	829.9	7.65	162570	156.89	27.44	208.06

[1] P_y = load at first yield of beam Δ_y = mid-span displacement at first yield of beam; P_u = peak load; $\Delta_{u,k}$ = mid-span displacement at peak load; M_u = ultimate moment; M_p= plastic moment of tested steel beam section; $M_{p\text{-uns*}}$= plastic moment of the unstrengthened beam without slab;k_s = effective pre-yield stiffness; Δ_u = mid-span displacement at ultimate state; and E_u = energy dissipated at ultimate state.

Table A2 FE results for steel I-beams for A572 specimens.[1]

Beam ID	P_y (kN)	$Ä_y$ (mm)	P_u (kN)	$Ä_{u,k}$ (mm)	M_u (kN.m)	M_p (kN.m)	M_u/ $M_{p\text{-uns*}}$	K_s (kN/mm)	$Ä_{u\,r}$(mm)	$ì_Ä$	E_u (kN·m)
A572-Beams without slab and 194 mm depth											
A572-B-194-NS-C	-	-	187.93	8.09	95.84	106*	0.90	-	8.09	-	-
A572-B-194-NS-S1	185.41	7.93	279.82	30.09	142.70	143.5	1.34	23380	87.61	11.04	20.03
A572-B-194-NS-S2	361.25	9.01	575.03	52.99	293.26	295.4	2.76	40094	151.13	16.77	78.84
A572-B-194-NS-S3	205.55	8.40	284.53	42.45	145.11	147.8	1.36	24470	88.77	10.56	22.48
A572-B-194-NS-S4	235.17	8.63	341.05	29.32	173.93	176.5	1.64	27250	85.33	9.88	28.81
A572-B-194-NS-S5	341.29	7.58	549.37	33.54	280.17	285.4	2.64	45025	151.22	19.94	75.23
A572-B-194-NS-S6	439.32	7.84	614.05	28.60	313.16	318.5	2.95	49696	154.65	19.72	84.43
A572-Beams with slab and 194 mm depth											
A572-B-194-S-C	279.18	7.34	368.96	40.98	188.16	189.7	1.77	38035	145.78	19.86	48.97
A572-B-194-S-S1	307.60	7.86	419.94	60.71	214.16	216.5	2.02	39134	147.18	17.39	56.32
A572-B-194-S-S2	444.34	8.35	734.08	51.19	374.38	376.9	3.53	53214	154.26	18.47	98.97
A572-B-194-S-S3	278.23	7.34	410.75	50.64	209.48	212.4	1.97	37905	155.05	21.12	58.06
A572-B-194-S-S4	326.01	7.57	526.96	69.75	268.74	270.1	2.53	43066	149.66	19.77	71.85
A572-B-194-S-S5	462.12	6.71	672.12	35.06	342.78	343.0	3.23	68870	155.56	23.18	92.19
A572-B-194-S-S6	507.02	5.75	777.19	23.74	396.36	397.5	3.73	88177	154.22	26.82	99.19

Table A2 Continued...

Beam ID	P_y (kN)	$\ddot{A}_y$ (mm)	P_u (kN)	$\ddot{A}_{u,k}$ (mm)	M_u (kN.m)	M_p (kN.m)	M_u/ $M_{p\text{-}uns*}$	K_s (kN/mm)	$\ddot{A}_{u\ r}$(mm)	$\grave{\imath}_{\ddot{A}}$	E_u (kN·m)
A572-Beams without slab and 350 mm depth											
A572-B-350-NS-C	-	-	248.88	3.02	126.92	141*	0.90	-	3.02	-	-
A572-B-350-NS-S1	384.11	7.34	525.97	58.21	268.44	269.9	1.90	52331	147.18	20.05	70.17
A572-B-350-NS-S2	496.31	6.33	1025.52	53.27	523.01	527.3	3.70	78406	154.03	24.33	148.33
A572-B-350-NS-S3	363.31	7.48	518.65	70.17	264.51	268.9	1.87	48570	151.14	20.20	71.85
A572-B-350-NS-S4	421.61	7.02	669.16	107.25	341.27	345.0	2.42	60058	150.78	21.47	91.59
A572-B-350-NS-S5	509.89	5.06	965.25	30.80	492.27	493.5	3.49	100768	151.07	29.85	139.31
A572-B-350-NS-S6	768.26	6.63	1163.17	21.63	593.21	594.5	4.20	115876	151.89	22.90	158.17
A572-Beams with slab and 350 mm depth											
A572-B-350-S-C	565.40	3.30	777.42	53.48	396.48	399.2	2.81	171333	149.81	45.39	103.30
A572-B-350-S-S1	572.31	3.34	839.81	81.21	428.30	430.1	3.03	171353	147.18	44.06	108.89
A572-B-350-S-S2	699.63	3.35	1689.28	51.02	861.53	865.6	6.11	208844	152.23	45.44	229.28
A572-B-350-S-S3	575.89	3.12	884.06	65.19	450.87	456.6	3.19	184540	152.39	48.84	117.66
A572-B-350-S-S4	718.54	5.02	1066.49	73.50	543.90	544.2	3.85	143135	151.91	30.26	148.23
A572-B-350-S-S5	1122.81	7.02	1614.16	32.87	823.22	826.1	5.83	159944	155.57	22.16	219.95
A572-B-350-S-S6	1421.57	7.66	1944.97	21.13	991.93	996.5	7.03	185583	156.89	20.48	246.77

[1] P_y = load at first yield of beam Δ_y = mid-span displacement at first yield of beam; P_u = peak load; $\Delta_{u,k}$ = mid-span displacement at peak load; M_u = ultimate moment; M_p= plastic moment of tested steel beam section; $M_{p\text{-}uns*}$= plastic moment of the unstrengthened beam without slab;k_s = effective pre-yield stiffness; Δ_u = mid-span displacement at ultimate state; and E_u = energy dissipated at ultimate state.